A line attractor maintains aggressiveness during feeding in "hangry" mice

Authors: Jineun Kim[1,2,3,*], Aditya Nair[4,5*], Nestor Coria[1,2], Sophia Huynh[1,2], Amit Vinograd[1,2,3], Jingyue Xu[1,2], Mengyu Liu[3,6] and David J. Anderson[3,§]

[1]Division of Biology and Biological Engineering

[2]Tianqiao and Chrissy Chen Institute of Neuroscience

California Institute of Technology

[3]Howard Hughes Medical Institute

Pasadena, CA, USA

[4]Lee Kong Chian School of Medicine, Nanyang Technological University, Singapore

[5]Institute of Molecular and Cellular Biology, Agency of Science, Technology and Research, Singapore

[6]Present address: Department of Bioengineering, Stanford University, Stanford, CA

Running Title: Effect of food deprivation on hypothalamic line attractor dynamics

*These authors contributed equally to this work

[§]Author for correspondence:

E-mail: wuwei@caltech.edu

SUMMARY

Aggression evolved to protect resources such as food from competitors, but animals must balance fighting and feeding so that they facilitate rather than hinder re-establishment of energy homeostasis. How this balancing is computed is not well understood. We have approached this problem at the level of neural population-coding by examining the effect of progressive starvation on a hypothalamic line attractor that encodes an internal state of aggressiveness. Moderate fasting yielded "hangry" mice, decreasing attack latency and increasing attack frequency. In parallel, line attractor ramping rate and stability were increased, suggesting that hunger enhances aggressiveness by modifying neural dynamics. In contrast, prolonged starvation inhibited aggression and eliminated the line attractor. In satiated mice, titrated acute chemogenetic activation of arcuate AgRP neurons recapitulated the biphasic effects of progressive starvation, suggesting that a continuous increase in hunger exerts bi-directional influences at different intensities. When confronted with food and an intruder, hangry mice alternated between feeding and fighting. During eating, population neural activity moved out of the line attractor while activity in the attractor dimension remained unchanged. Following feeding, activity rapidly relaxed back into the attractor and aggression resumed. Thus, the line attractor may serve to keep hungry animals primed for aggression during intermittent feeding bouts.

Keywords | Dynamical systems analysis, interacting internal states, hunger, aggression, emotion, homeostasis, flexible innate behaviors, state-dependent modulation

INTRODUCTION

Aggression evolved to protect resources essential for individual survival and reproduction such as food, territory, mating partners, or offspring[1]. However, fighting is mutually exclusive with behaviors that mediate resource acquisition and consumption. Thus, for example, hungry animals must dynamically adjust their choice between feeding and fending off competitors for food so that fighting facilitates, but does not ultimately interfere with, re-establishment of energy homeostasis[2-5]. This choice likely depends upon multiple factors such as residual energy reserves, quantity and quality of food resources and perceived aggressiveness of the competitor. How this dynamic decision-making is computed by the brain to optimize flexible behavioral prioritization[6] is not well understood.

As a first step towards addressing this question, we have investigated how aggressive behavior and brain activity are modulated by the duration of starvation. Hunger is well-known to enhance aggressiveness in multiple species[7-10], and is experienced in humans as "hanger"[11-13]. Surprisingly, this phenomenon has not been convincingly demonstrated in mice. To the contrary, recent data suggest that food deprivation inhibits rather than enhances aggression in mice[5,14]. Older studies have described bi-directional effects of fasting duration on aggression[15], but characterization of these effects was limited.

Aggression is controlled by estrogen receptor-1 (Esr1)[16]- and progesterone receptor (PR)[17,18]- expressing neurons located in the ventrolateral subdivision of the ventromedial hypothalamic nucleus (VMHvl[19]; reviewed in refs[20-22]). VMH is also a well-known neural hub for controlling feeding and metabolic regulation[23-25]. Whether and how hunger controls aggression via influences on VMHvl$^{Esr1/PR}$ neurons is not clear. A suppressive effect of starvation on aggression was shown to be mediated by VMHvl-projecting BNST neurons that receive inhibitory input from NPY-responsive medial amygdala (MeA) neurons[14], but the role of VMHvl$^{Esr1/PR}$ neurons was not investigated.

Given the complexity of VMHvl cell types[26-29], circuitry[25,30-32] and single-unit activity[19,33,34], we have asked whether aggressiveness is modulated by food deprivation at the level of population coding and manifolds in neural state-space[35-39]. Attractors are a

well-established population coding mechanism for computing cognitive variables[39-44]. Recently, we identified an approximate line attractor[45] that encodes a scalable and persistent internal state of aggressiveness in VMHvl[46-48]. Other data suggest that attractor dynamics may encode physiological internal states as well[49]. For example, competition between feeding and drinking is reflected in dynamical interactions between apparent basins of attraction for hunger vs. thirst[50,51].

Here we report that different durations of starvation exert strongly correlated bi-phasic influences on aggressiveness and on VMHvl^{Esr1} line attractor dynamics, an effect recapitulated by titrated short-term chemogenetic activation of arcuate AgRP-expressing "hunger"-promoting neurons[52-54] in satiated mice. Furthermore, activity in this line attractor remains persistently elevated when "hangry" mice alternate between feeding and attack bouts in a behavioral choice paradigm. These results suggest that modifications of VMHvl line attractor dynamics may underlie the neural coding of "hanger," and that this attractor may play an adaptive role to keep hungry animals "primed" for attack while replenishing their energy reserves.

RESULTS

Metabolic states modulate male aggression in a biphasic manner, establishing hunger-enhanced aggression in mice

To determine the features of aggressive behaviors in male mice that are modulated by metabolic states, we employed the standard resident-intruder (RI) assay[33,55] and perturbed the resident's energy states by limiting food availability with different durations of food deprivation before introducing a rival (*ad libitum*-fed) intruder (Fig. 1a). The same resident mice under *ad libitum* feeding conditions served as within-subject controls, using a cross-over design (Fig. 1b). The RI assay itself was performed in the resident's home cage in the absence of food.

Mice that were food-deprived for 18 hours exhibited heightened aggression compared to those fed *ad libitum*, as evidenced by a significant increase in time spent attacking[6], the number of attack bouts, and a reduction in inter-attack bout interval

duration (although there was no change in average attack-bout duration; Fig. 1c-f). In addition, the probability of attack following the initial aggressive encounter increased under starvation (Fig. 1g). Notably, 18h-fasted mice showed a significantly shorter latency to initiate the first attack than the same mice under *ad libitum*-fed conditions (Fig. 1h, i).

We also investigated whether there were additional changes in the kinematics[56] of aggressive behavior under starvation. We employed machine learning (ML) to quantify the intensity of aggression based on the values of different pose estimation[57]-derived features, using seven key points assigned to each mouse (Fig. 1j; see Methods). Among these features, we found that pixel change, a measure of movement velocity across frame[57] (Fig. 1j, right-black), was significantly higher during aggression performed by 18-hr-fasted mice compared to *ad libitum*-fed controls (Fig.1k, bar graph). This increase was observed specifically during video frames annotated as attack bouts, but not during sniffing bouts (Fig. 1k vs. 1l). This result corroborates our subjective impression that aggression in mice fasted for 18 hours was more vigorous compared to that in fed animals.

We next sought to reconcile this observation with prior studies demonstrating that food deprivation suppressed aggression in male mice[6,14]. This apparent discrepancy could reflect methodological differences or dynamic biological interactions between hunger and aggression states. To investigate whether the effect of hunger to promote aggressiveness was a linear function of starvation time, we measured aggression after shorter (~8 hr) or more extended (40 hr) periods of food deprivation. (The durations were chosen based on body weight changes and compatibility with similar zenithal times for performing behavioral assays; Extended Data Fig. 1a, Methods.) Mild starvation (8 hr) did not significantly alter aggressive behavior compared to the fed states (Extended Data Fig. 1b, c). In contrast, prolonged starvation (40 hr) dramatically attenuated aggressive behavior, consistent with previous reports[14,15], and significantly increased attack latency compared to *ad libitum*-fed mice (Extended Data Fig. 1d, e). Notably, the time spent investigating male intruders was not significantly different across different energy states, although there was a trend to increased sniffing after 40 hours of food deprivation (Extended Data Fig. 1f; see also Fig. 3c and Extended Data Fig. 2a). Thus, food

132 deprivation had a biphasic effect on aggression in mice, with intermediate starvation
133 enhancing and prolonged starvation decreasing aggressive behavior[15].

134 We also observed a profound change in male sexual behavior during interactions
135 with female mice under intermediate fasting conditions[6] (Extended Data Fig. 1g). In the
136 absence of food, male mice exhibited a marked decrease in sexual behavior (such as
137 mounting and intromission toward female intruders) following 18 hours of fasting,
138 suggesting that a deviation from metabolic homeostasis can suppress sexual drive under
139 some conditions (Extended Data Fig. 1h-m). Remarkably, under these conditions, 20% of
140 males even displayed aggressive behavior toward female intruders, a behavior rarely
141 observed under *ad libitum*-fed conditions (Extended Data Fig. 1h-pie chart). This
142 observation underscores the potency of 18 hours of fasting to alter the balance of social
143 behaviors, increasing aggression while decreasing mating.

144 **Intermediate starvation alters the ramping and stability of line attractor dynamics**
145 **representing the aggressive state**

146 We next sought to characterize neural correlates underlying the hunger-induced
147 enhancement of aggressiveness; in other words, how is the internal state colloquially
148 termed 'hanger' encoded in the brain[46,47]? To this end, we measured the activity of
149 individual VMHvl^{Esr1} neurons expressing GCaMP8m by performing *in vivo*
150 microendoscopic calcium imaging[58] in mice fed *ad libitum,* and in the same mice following
151 18 hours of food deprivation. This longitudinal imaging allowed us to track the same
152 population of neurons over several days (see Methods) to examine changes in their
153 relative activity across distinct energy states (Fig. 2a-d). We confirmed that mice with
154 GRIN lens implants and head-mounted miniature microscopes recapitulated the
155 phenotypic readouts of hunger-induced changes in aggressive behaviors (Extended Data
156 Fig. 2a-e).

157 First, we investigated whether 18hr-fasting caused changes in overall neural
158 activity or in the behavioral tuning of individual neurons. The mean, peak z-score activity,
159 and time to peak of z-score activity of all VMHvl^{Esr1} neurons following the first sniff were
160 not statistically different between fasted and fed mice (Extended Data Fig. 2f-j). Choice

161 probability analysis of single-neuron behavioral tuning[33] confirmed that most neurons
162 (>70%) exhibited mixed selectivity for male-directed behaviors in both the fed and 18-hr
163 fasted states (Extended Data Fig. 2k, l, gray), consistent with prior findings in *ad libitum*-
164 fed mice[33,48,55]. Among behavior-tuned cells, the percentage of sniff- or attack-tuned
165 VMHvl^{Esr1} neurons was not significantly different in fed versus fasted mice (Extended
166 Data Fig. 2k-m, q). Furthermore, the mean activity (post-sniff) of attack-tuned or sniff-
167 tuned populations was not affected by starvation (Extended Data Fig. 2n-p, r-t). Thus,
168 analysis of single-unit activity and behavioral tuning in VMHvl^{Esr1} neurons failed to reveal
169 robust changes that correlated with the increased aggressiveness of 18 hr-starved mice.

170 We next investigated whether changes in the population coding of behavior could
171 be observed between fed and 18hr-fasted mice. As a first step, we used generalized
172 linear models (GLMs). Previous studies in females have indicated that GLMs using
173 behavioral regressors do not explain a high fraction of the variance in VMHvl^{Esr1} neural
174 activity[59]; we confirmed the same was true for activity in both fed and fasted males
175 (Extended Data Fig. 3a, b). While inclusion of a cell-to-cell coupling term (which
176 incorporates correlations in activity among VMHvl^{Esr1} neurons) in the GLM increased the
177 model fit[59-61], the mean variance in neural activity explained was still <50% in both
178 conditions (Extended Data Fig. 3c-f), a relatively poor fit.

179 Because the coupling term may reflect local connectivity, and since neural
180 dynamics can be influenced by local connectivity[62], we next examined whether neural
181 dynamics were altered by 18hr food deprivation. One measure of neural dynamics is
182 their decay time following peak activity. To assess this, we calculated the autocorrelation
183 half-width (ACHW)[33,63,64], a proxy for single-neuron persistence, for each neuron across
184 both conditions. This revealed a small but statistically significant increase in decay time
185 in 18hr fasted mice in the bulk VMHvl^{Esr1} population (Extended Data Fig. 3g-j, mean
186 ACHW: 9.7± 0.3s for fed state vs 11.58 ± 0.3s for fasted state, p****<0.0001, n=6 mice).

187 As VMHvl^{Esr1} neurons are heterogeneous[26], we investigated next whether there
188 were latent subpopulations of neurons in this population that might exhibit more robust
189 changes in dynamics than the population as a whole, following food deprivation. To do

190 this, we applied an unsupervised probabilistic modeling approach, recurrent Switching
191 Linear Dynamical Systems (rSLDS)[65,66]. This approach uses dimensionality reduction to
192 identify latent dimensions (factors) in VMHvl^{Esr1} population activity that differ in their
193 activity and dynamics. It then fits a linear dynamical system model to activity in this latent
194 dimension state-space, using machine learning (Extended Data Fig. 4a). Consistent with
195 prior studies[46,59], rSLDS models fit to data from both fed and 18 hr-fasted mice explained
196 a much larger fraction of the variance in neural activity (cvR^2 $\geq$90%; Fig. 2e) than was
197 explained by GLMs.

198 To interpret these models, we examined the "learned" dynamics matrix *A* of the
199 longest-lived state, fit by the model (Extended Data Fig. 4a). The eigenvalues of this
200 matrix yield the time constants of each of the latent dimensions[65,66]. Consistent with our
201 earlier studies[46-48,59], models fit to data from fed mice yielded one dimension (X_1) with a
202 substantially greater time constant than the next-slowest dimension (X_2), suggestive of a
203 "slow mode," or integration dimension (Fig. 2f-i, o; Extended Data Fig. 4g). This slow
204 mode is characterized by "ramping up" behavior during sniffing episodes, reaches its
205 peak level at the onset of attack, remains elevated between attack bouts and decays
206 slowly thereafter[46] (Fig. 2f-i, burgundy curves; Extended Data Fig. 4b). In contrast, the
207 orthogonal (X_2) dimension exhibited transient activity that peaked at the first sniff and then
208 declined rapidly (Fig. 2f-l, gray curves; Extended Data Fig. 4c). In 2D flow-field
209 visualizations of the state-space model, the X_1 dimension yielded a linear region of "slow
210 points" that may represent a leaky integrator or approximate line attractor[46,47] (Fig. 2r, s;
211 Extended Data Fig. 4h, dashed lines). rSLDS models fit to data from 18 hr fasted mice
212 yielded a qualitatively similar result, in terms of latent factors and their dynamics (Fig. 2g,
213 i).

214 To determine whether line attractor parameters differed quantitatively between fed
215 and 18 hr-fasted mice, we compared the ramping and decay phases of the projected X_1
216 integration dimension activity under the two conditions. Alignment of normalized z-scored
217 activity to the onset of the first attack revealed significantly steeper ramping dynamics in
218 fasted vs. fed mice (Fig. 2j$_i$). Importantly, comparison of raw z-scored activity indicated
219 that this faster ramp-up was due to a steepening of the slope rather than to a reduction in

220 absolute peak X_1 activity (Fig. 2j_{ii}, inset; Extended Data Fig. 4d, e_{ii}). This faster ramp-up
221 in starved mice mirrored the reduced latency from the first sniff to the first attack in this
222 condition (Fig. 1h, I; Extended Data Fig. 4e_i). Indeed, these two parameters were strongly
223 and significantly correlated both within and across mice (Fig. 2; Extended Data Fig. 4e,
224 f). Thus, 18-hr food deprivation caused a change in neural dynamics during the transition
225 from sniff to aggression, not a lowering of the threshold level of X_1 activity associated with
226 attack (Fig. 2l).

227 Our previous studies have shown that following ramp-up, activity in the line
228 attractor remains at a stable position during attack and then slowly decays back down the
229 attractor after the intruder is removed and fighting stops[46]. Importantly this decay
230 constant is highly correlated with the intensity of aggressiveness across individual
231 mice[46,48]. We therefore investigated whether the increased duration and frequency of
232 attack in 18 hr-starved mice might be reflected in an increased stability of the line attractor.
233 Indeed, activity in the X_1 dimension following the termination of attack decayed more
234 slowly in fasted than in fed mice (Fig. 2m, n), reflecting a significant increase in both the
235 absolute magnitude of the X_1 time constant, and in the X_1:X_2 time constant ratio (Fig. 2o;
236 Extended Data Fig. 4g). Consistent with this, the ACHWs of neurons strongly weighted
237 on the X_1 dimension were significantly longer in fasted than in fed mice (Fig. 2p, q, mean
238 ACHW: 11.6 ± 0.6s for fed state vs 14.9 ± 0.7s for fasted state, p***=0.0006, n=6 mice),
239 and were greater than in the bulk VMHvl^{Esr1} population (Fig. 2q vs. Extended Data Fig.
240 3j). Taken together, these data indicate that the effect of 18-hr fasting to increase
241 aggressive behavior is correlated with changes in two dynamic X_1 parameters: faster
242 ramp-up and slower decay along the attractor.

243 In 2D flow field maps of neural state space, under both conditions the trajectory of
244 the latent factor activity vector reached the end of the line attractor when attack
245 commenced (Fig. 2r_{ii}, s_{ii}). However, the initial trajectory was different with respect to the
246 X_2 dimension in fasted mice, initially following a path at an acute angle to the attractor
247 before relaxing to the line itself, rather than moving up the attractor as in fed mice (Fig. 2r
248 vs. 2s; Extended Data Fig. 4h). The raw activity and initial dynamics in the X_2 dimension
249 appeared similar in both conditions, although there was a trend to lower X_2 peak activity

250 in fasted mice (Extended Data Fig. 4c). Activity in X_2 may represent novelty or social
251 fear[46], and is known to interact with X_1[47]; it is possible that the strength of this interaction
252 is enhanced by starvation.

253 **Prolonged fasting reveals a biphasic effect of food deprivation on the stability of**
254 **VMHvl^{Esr1} attractor dynamics**

255 Changes in neural dynamic parameters and behavioral metrics observed between
256 *ad libitum*-fed and 18-hr fasted mice indicate that moderate food deprivation robustly
257 enhances both measures, consistent with the 'hangry' state described in humans[12,13] and
258 other species[7,8,9 ,15]. To reconcile this with reports that starvation suppresses aggression
259 in mice[6,14] and with our finding that prolonged fasting (40 hr) markedly reduces aggression
260 (Extended Data Fig. 1d), we next examined neural population dynamics under this latter
261 condition (Fig. 3a).

262 First, we confirmed that *Esr1*$^{Cre/+}$ mice implanted with a GRIN lens and miniscope
263 responded to 40-hr starvation like wild-type unoperated mice, exhibiting a marked
264 decrease in aggressive, but not investigatory, behaviors (Fig. 3b, c). rSLDS modeling
265 revealed that, in contrast to the 18-hr fasted condition (Fig. 3f$_i$-burgundy, g-blue), activity
266 projected onto the X_1 dimension in 40-hr fasted animals exhibited rapid decay following
267 the first sniffing bout (Fig. 3e, f$_{ii}$-burgundy, g-purple, h). Accordingly, the time constant of
268 the X_1 dimension was not significantly greater than that of X_2 dimension (Fig. 3i, inset),
269 and was markedly reduced relative to both the 18-hr fasted condition (Fig. 3i, j$_i$; 18-hr vs.
270 40-hr) and *ad libitum*-fed controls (Fig. 3j$_i$; 0 vs. 40-hr). The same was true for the ratio
271 between the time constants of X_1 and X_2 (Fig. 3j$_{ii}$).

272 In agreement with these changes in latent factor dynamics, analysis of ACHWs in
273 X_1-weighted neurons identified using the emission matrix demonstrated reduced
274 persistence and shorter decay times in 40-hr starved vs. the 18-hr fasted and fed states
275 (Fig. 3k). Concordantly, 2D vector flow-field visualizations of rSLDS models from 40-hr
276 fasted mice failed to exhibit a well-defined linear region of slow points (Fig. 3l, cf. Fig. 2r,
277 s). Collectively, these data suggest that in 40-hr fasted mice, the line attractor is either
278 absent or is considerably “leakier” than that in either *ad libitum*-fed or 18-hr fasted mice.

279 These findings reveal a biphasic, bi-directional effect of hunger on aggression, which is
280 reflected by a corresponding biphasic change in line attractor dynamics (Fig. 3m).

281 **Titrated activation of hunger-promoting neurons modulates aggression and**
282 **VMHvl^{Esr1} attractor dynamics, recapitulating effects observed during naturalistic**
283 **food deprivation.**

284 Our results revealed a robust interplay between starvation and aggression at the
285 level of population dynamics in VMHvl^{Esr1} neurons. We next investigated whether the
286 opposite-direction effects of food deprivation on aggressiveness at 18 vs. 40 hr reflected
287 a change in the effects of a graded hunger motivational state at different intensities, or
288 rather the gradual depletion of energy resources or weight loss after extended starvation.
289 To distinguish between these possibilities, we tested whether acute, graded activation of
290 hypothalamic 'hunger' neurons[50,54,67] at different intensities in *ad libitum*-fed mice could
291 recapitulate the starvation-induced biphasic effects of starvation on aggressive states and
292 population neural dynamics.

293 To this end, we employed titrated chemogenetic activation of AgRP-expressing
294 neurons in the arcuate nucleus (ARC^{AgRP} neurons); these neurons promote a hunger drive
295 in response to interoceptive cues that signal reduced bodily energy state[50,52-54,68].
296 Previous studies have demonstrated that graded changes in the intensity of ARC^{AgRP}
297 neuronal activation produced correspondingly graded increases in food intake[53,69].
298 Although strong activation of these neurons moderately affects aggression[6,14], whether
299 titrated activation can yield bi-directional effects at different intensities has not previously
300 been investigated. To test this, we systemically administered deschloroclozapine (DCZ),
301 a metabolically stable and fast-acting DREADD agonist, at different calibrated doses (0,
302 [saline control], 0.1, 0.5, 1.0 mg/kg)[70] on different days to *ad libitum*-fed AgRP$^{Cre/+}$ mice
303 injected with AAV-FLEX-hM3Dq-mCherry into the ARC 40 min prior to conducting RI
304 assays (Fig. 4a; see Methods).

305 At the lowest dose of DCZ (0.1 mg/kg), there was no significant effect on attack-
306 related parameters compared to the control condition; however, there was a marginal
307 reduction in the latency to initiate feeding, indicating the efficacy of chemogenetic
308 activation of ARC^{AgRP} neurons even at this relatively low dose (Fig. 4b-d, 0.1mg/kg). In
309 contrast, at an intermediate dose (0.5 mg/kg), mice displayed a significantly shorter

310 latency to the first attack as well as a marked increase in the time spent attacking (Fig.
311 4b, c, 0.5mg/kg), resembling "hangry" mice. The latency to initiate feeding was further
312 reduced, resulting in virtually immediate engagement in feeding behavior upon food
313 presentation in the absence of an intruder male (Fig. 4d, 0.5 mg/kg). In contrast, at the
314 highest dose of DCZ tested (1 mg/kg), aggressive behaviors were markedly suppressed,
315 and animals exhibited an immediate initiation of feeding upon food presentation (Fig. 4b-
316 d, 1 mg/kg). Thus, titrated chemogenetic activation of ARC^{AgRP} neurons recapitulated the
317 biphasic, bi-directional effect of progressively increased durations of food deprivation on
318 aggression (Fig. 4b, c; see also Fig. 3b and Extended Data Fig. 1d).

319 Next, to assess whether and how the graded activation of ARC^{AgRP} neurons
320 modulates attractor dynamics in $VMHvl^{Esr1}$ neurons, we combined miniscope imaging of
321 $VMHvl^{Esr1}$ neurons with titrated chemogenetic activation of ARC^{AgRP} neurons (Fig. 4e, f).
322 Specifically, we expressed a Flp-dependent GCaMP8m calcium indicator in $VMHvl^{Esr1}$
323 neurons and a Cre-dependent FLEX-hM3Dq-mCherry virus in ARC^{AgRP} neurons of
324 $AgRP^{Cre/+}$; $Esr1^{Flp/+}$ double-transgenic mice (Fig. 4e). $VMHvl^{Esr1}$ neural activity was
325 longitudinally recorded across multiple days under three experimental conditions: mice
326 were subjected to systemic administration of saline (control), 0.5mg/kg (medium), and
327 1mg/kg (high) doses of DCZ in a physiologically *ad libitum*-fed state, using a counter-
328 balanced design across conditions (Fig. 4f), and calcium signals were acquired during an
329 RI assay 40 minutes following drug administration. Social behaviors were measured in
330 synchronized video recordings (Extended Data Fig. 5a, blue and red rasters).

331 rSLDS models fit to $VMHvl^{Esr1}$ neural population activity recorded at different DCZ
332 doses yielded consistently high cvR^2 values across all tested conditions (Fig. 4g). Notably,
333 quantitative changes in dynamic parameters of the two latent dimensions revealed by
334 rSLDS modeling during titrated activation of ARC^{AgRP} neurons closely mirrored the
335 biphasic dynamical changes observed under naturalistic food-deprivation conditions (Fig.
336 4h-i vs. 4k-l). Specifically, under control (saline-injected) conditions, activity along the X_1
337 dimension progressively ramped up before the initiation of the first attack (Fig. $4h_i$;
338 Extended Data Fig. 5a-left, 5c-gray), similar to *ad libitum*-fed un-injected control mice (Fig.
339 $4k_i$). Activation of ARC^{AgRP} neurons at the medium DCZ dose, when mice showed the

340 shortest latency to attack behavior (Fig. 4b; 0.5 mg/kg), yielded more rapid ramping
341 followed by sustained activity in the X_1 dimension (Fig. 4h_{ii}-burgundy; Extended Data Fig.
342 5a-middle, 5b, c-d (pink), 5d-e), resembling the X_1 activity pattern in the 18-hr fasted
343 condition (Fig. 4k_{ii}). Aligning neural trajectories along the X_1 dimension to the onset of the
344 initial sniff revealed a significantly accelerated ramping rate in the medium-dose condition
345 compared to controls (Extended Data Fig. 5a; left vs. middle and 5c-e). Remarkably, the
346 latency to attack was almost perfectly correlated across mice with the time-to-peak of
347 projected X_1 activity in the medium-dose condition (Extended Data Fig. 4f; R^2 = 0.98,
348 p*=0.045). This correlation was even stronger than that observed under 18 hour of food
349 deprivation (R^2 = 0.85; Fig. 2k; Extended Data Fig. 4f-left), perhaps reflecting the more
350 precise control over hunger levels achieved by chemogenetic activation of ARC^{AgRP}
351 neurons.

352 In contrast, during chemogenetic activation of ARC^{AgRP} neurons at the highest
353 dose tested (1 mg/kg), rSLDS analysis revealed a pronounced reduction in the
354 persistence of activity along the X_1 dimension, reflected in a rapid decay following initial
355 sniff (Fig. 4h_{iii}-burgundy; Extended Data Fig. 5a-right, 5g-dark red). This rapid decay
356 resembled the faster dynamics observed in the prolonged starvation condition (Fig. 4k_{iii}),
357 and was reflected by a reduced magnitude of the X_1 time constant remarkably similar to
358 that seen under 40 hr starvation (Fig. 4i, l; Extended Data Fig. 5l). Notably, both the
359 persistence of X_1 activity, quantified as the area under the curve (AUC) following the initial
360 sniff, and the ACHWs of X_1-weighted neurons, were significantly diminished in the high-
361 dose DCZ condition, compared to the medium-dose (0.5 mg/kg) condition (Fig.4j;
362 Extended Data Fig. 5g, h, k). These dose-dependent biphasic effects were further
363 underscored by changes in the ratio of the X_1 to X_2 time constants (Extended Data Fig.
364 5i, j, m), highlighting a graded, biphasic modulation of attractor stability by scaled hunger
365 levels.

366 Consistent with the observed DCZ dose-dependent changes in these fit rSLDS
367 model parameters, neural trajectories visualized in a two-dimensional flow-field state
368 space under the medium-dose condition closely resembled those observed after 18 hours
369 of fasting, with prominent line attractors in both conditions (Extended Data Fig. 6a vs. 6b).

370 In contrast, the trajectories under the high-dose condition exhibited disrupted attractor
371 dynamics reminiscent of those following 40 hours of fasting, characterized by a loss of
372 clearly defined linear regions of slow points (Extended Data Fig. 6c vs. 6d). Changes in
373 the ACHWs of individual X_1 dimension-weighted neurons under titrated chemogenetic
374 AgRP neuron activation similarly paralleled the changes observed under naturalistic food
375 deprivation states (Fig. 4j vs. 4m).

376 Thus, graded activation of ARC^{AgRP} neurons in *ad libitum*-fed mice reproduced the
377 bi-phasic changes in both aggressive behavior and the dynamics of $VMHvl^{Esr1}$ neuronal
378 activity observed with different durations of food deprivation (Fig. 4n; Extended Data Fig.
379 6e). These data argue against the idea that the reduced aggression observed after 40 hrs
380 of starvation is due simply to energy depletion or weight loss and imply that increasing
381 intensities of a unitary starvation state are converted into opposite-direction modulation
382 of aggressiveness and line attractor properties at distinct thresholds. They further suggest
383 that the VMHvl line attractor constitutes a key integrative node where metabolic and
384 motivational signals converge to regulate aggressiveness, likely through state-dependent
385 modulation of underlying population dynamics. While we cannot formally exclude that
386 hunger-induced changes in line attractor dynamics might be a consequence rather than
387 a cause of changes in aggressive behavior, this seems unlikely given that the line attractor
388 is present in mice passively observing, as well as actively engaging in, attack behavior[47],
389 and that it persists in 'hangry' mice in which attack is interrupted by feeding (see below).

390 **Increased line attractor stability in 'hangry' mice maintains aggressiveness during**
391 **feeding**

392 The above results establish that a graded hunger state can either enhance or
393 suppress aggressiveness and line attractor dynamics, depending on its intensity. Given
394 that aggression is energetically costly[71] and mutually exclusive with feeding, these
395 findings prompted us to ask two related questions: 'Why does an intermediate level of
396 hunger elevate aggression?', and 'Why is this increase in aggressiveness encoded in the
397 enhanced stability of a line attractor, rather than simply by an increased activity in
398 aggression-promoting neurons?' To tackle these questions, we further examined attractor
399 dynamics under conditions in which 18-hr fasted animals were allowed to choose

400 between feeding and attacking an intruder. To this end, following an approximately 2-min
401 RI test to assess the resident's baseline level of aggressiveness, we introduced a chow
402 pellet without removing the intruder (Fig. 5a). After imaging neural activity and observing
403 behavior for two minutes in the presence of both the food and the intruder, we removed
404 the intruder but left the food pellet in place (to determine whether the resident was satiated
405 or still hungry). This design allowed us to examine the animal's behavioral choices under
406 conditions of competing hunger and aggressive drive states, with targets of both
407 consummatory behaviors concurrently provided.

408 Following the introduction of the chow pellet, 'hangry' mice immediately stopped
409 fighting, investigated the pellet, and ate (Fig. 5b, d-left). In contrast, relatively little feeding
410 was observed in *ad libitum* fed animals, as the chow pellet only yielded brief interruptions
411 of attack (Fig. 5b, c). In the 18-hr fasted mice, following a period of feeding (~100 s), 67%
412 of the fasted mice resumed attacking the intruder (Fig. 5d-right; Extended Data Fig. 7a,
413 b-pie chart). However, their latency to resume attack was marginally longer than in the *ad*
414 *libitum*-fed control condition (mean latency to resume attack after the offset of the first
415 food sniff (s): 137 ± 26 s (fasted) vs. 94 ± 24 s (fed), p=0.06) (Fig. 5d; Extended Data Fig.
416 7b). Following the initial re-attack, 18-hr fasted mice resumed feeding and continued with
417 interspersed feeding and attack bouts (Fig. 5d-right; Extended Data Fig. 7a). Overall, the
418 fasted mice spent far more time feeding than attacking (percent time spent eating vs.
419 attacking in fasted state: 32.7 ± 4.42 % (eating) vs. 3.37 ± 0.67 % (attacking), ****p<0.001;
420 in fed state: 3.2 ± 3.7 % (eating) vs. 3.7 ± 1.3 % (attacking), p=0.882, Fig. 5e; Extended
421 Data Fig. 7a-right). Nevertheless, under these conflicting conditions mice did not achieve
422 satiety, as indicated by extensive feeding following removal of the intruder (Fig. 5f, yellow
423 raster). These findings reveal a dynamic and hierarchical interplay between two
424 competing motivational states and suggest that mice are willing to delay or sacrifice full
425 repletion of their energy reserves in order to defend their food resource from a competitor
426 male.

427 We next sought to determine how neural activity and dynamics in VMHvl^{Esr1}
428 neurons might be modulated during the observed dynamic switching between fighting
429 and feeding. Unexpectedly, hierarchical clustering as well as choice probability analysis

of single VMHvl^{Esr1} neuron activity revealed a robust population of eating-tuned neurons in 18hr fasted mice (Fig. 5f-h). Consistent with this observation, a larger fraction of variance in neuronal activity could be explained by a behavior-weighted GLM in fasted mice during interactions with food and a male, compared to GLMs fit to the same mice in the absence of food but presence of male (mean cvR^2 in fasted mice with food: 27% variance explained, Extended Data Fig. 7c$_i$; mean cvR^2 in fasted mice without food: 17% of variance explained, Extended Data Fig. 3b, lower), likely reflecting the behavior-locked activity of the eating-tuned population (see below; Fig. 5h). Nevertheless, the addition of a cell-coupling term still increased the variance explained by GLMs in the presence of food (mean cvR^2: 0.27 with only behavioral regressors, cvR^2: 0.52 with behaviors and cell-coupling, Fig. 5i; Extended Data Fig. 7c$_{ii}$). This suggests that local functional connectivity between neurons - and therefore potentially neural dynamics - influences population activity in this paradigm as well.

To directly examine neural dynamics in this competition paradigm, we fit rSLDS models to VMHvl^{Esr1} activity. In this condition, models with three dimensions instead of two explained a greater fraction of neural variance in data (66.3 ± 4% variance explained for the 3D model vs. 44.1 ± 2% variance explained for the 2D model, Extended Data Fig. 7d). To understand the behaviors represented by these three latent factors, we analyzed their projected time-varying activity during sniffing, attack, and eating (Fig. 5j; Extended Data Fig. 7e, f). The X_1 dimension exhibited ramping activity that peaked near the attack onset and persisted thereafter (Fig. 5j, k, l$_i$, m$_i$-burgundy; Extended Data 7e, f, X_1), as previously described[46]. Interestingly, despite the switch of overt behavior from attacking to eating, the level of activity in the X_1 dimension remained stable and elevated during food sniffing and consumption (Fig. 5j, k, l$_{ii-iii}$, m$_{ii-iii}$, burgundy; Extended Data Fig. 7e, f, X_1). Notably, when animals resumed attacking, activity in the X_1 dimension was similar to that observed during the initial attack (Fig. 5l$_{iv}$, m$_{iv}$; Extended Data Fig. 7e, f, X_1 and 7i). By contrast, activity in the X_2 dimension declined following the initial male interaction and remained relatively low throughout aggression, feeding and re-attack (Fig. 5j, k, l$_{i-iv}$, m$_{i-iv}$-gray; Extended Data Fig. 7e, f, X_2).

In contrast to these first two dimensions, the X_3 dimension, enriched in food-modulated neurons (Fig. 5j, X_3), displayed little activity during male interactions before the delivery of the food pellet, but exhibited time-locked, transient increases in activity during feeding bouts (Fig. 5l_{ii}-arrowhead, 5m_{ii}-green; Extended Data Fig. 7e, f, X_3). Following the offset of eating, the X_3 dimension displayed rapid decay, unlike the slow decay observed in the X_1 dimension (Fig. 5l_{iii}-arrowhead, n), reflecting distinct dynamics across these two dimensions of activity.

These results indicate that activity in the X_1 line attractor-aligned dimension remained stably elevated as the animal switched back and forth between attacking and eating (Extended Data Fig. 7g). Indeed, a decoder trained on the activity of the X_1 dimension was unable to distinguish video frames containing attack vs. eating (Fig. 5o), whereas a decoder trained on the activity of the X_3 dimension robustly distinguished attack vs eating frames (Extended Data Fig. 7h). In line with this population-level dissociation, neurons with strong weights onto the X_3 dimension exhibited significant tuning for eating, whereas neurons contributing to the X_1 and X_2 dimensions were preferentially tuned to male-directed behaviors (Extended Data Fig. 7i, j).

To visualize the dynamics of these three dimensions in neural state space, we first plotted the fit rSLDS state-space model as a vector flow field spanned by the X_1-X_2 dimensions. In this space, we observed that the population vector remained in the line attractor during bouts of eating as well as attack (Extended Data Fig. 8a-d). In contrast, the fit vector flow field spanned by the X_1-X_3 dimensions revealed that the population vector displayed movements orthogonal to the line attractor and parallel to the X_3 dimension during eating but returned to the line attractor immediately when the animals switched back to attack (Extended Data Fig. 8e-h).

Together, these findings revealed that neural population dynamics in the VMHvl^{Esr1} neurons of mice in a behavioral choice paradigm exhibited a persistently elevated component of activity in the X_1 (line attractor) dimension, despite repeated switches between attack and eating. Transitions to eating engaged an orthogonal dimension (X_3), which (in contrast to X_1) displayed rapid decay following the offset of feeding. As attack

488 resumed following such feeding bouts, activity in the line attractor dimension dominated
489 over that in the orthogonal dimensions (X_2 and X_3) (Fig. 5p-r).

490 **DISCUSSION**

491 While VMHvl is well-known to regulate both social behaviors[20,22,72] and feeding[73,74],
492 relatively few studies have investigated how these two functions influence each other[21]
493 and none has done so at the level of neural population activity. Here we have investigated
494 how aggressiveness and neural dynamics are influenced by hunger in VMHvl. We find
495 that starvation exerts bi-phasic, opposite-direction effects on aggression depending on
496 the duration of food deprivation[6,14,15], and that these bi-phasic effects are reflected in bi-
497 phasic changes in line attractor dynamics[46] rather than in overall levels of activity among
498 VMHvl^{Esr1} neurons. For example, our analysis suggests that 'hangry' mice do not have a
499 "shorter fuse" than fed mice, as intuition might suggest; rather, their "fuse" is the same
500 length, but burns faster (increased ramping rate from baseline to peak in the X_1
501 dimension). Together, our observations reveal how population neural dynamics that
502 encode aggressiveness, an affective or emotional internal state[75], can be modified by a
503 competing homeostatic physiological drive state[76,77].

504 Importantly, the bi-phasic effects of food deprivation on aggressiveness and line
505 attractor dynamics could be replicated by acute, titrated chemogenetic activation of
506 ARC^{AgRP} neurons[52,53] in sated mice. This finding argues that these bi-directional effects
507 reflect different intensities of a graded hunger state[5,78], and that the loss of
508 aggressiveness after 40 hrs of starvation[5,6,14] is not due simply to gradual depletion of
509 energy reserves or to weight-loss. These observations make sense from an ecological
510 perspective[79]. In this view, the level of risk the animal is willing to tolerate scales with the
511 intensity of its starvation state: if moderately hungry, the animal will fight to protect its food
512 supply, risking further energy depletion (and injury or death if defeated). With extended
513 starvation, however, the animal prioritizes food consumption, during which time it is
514 vulnerable to attack. The circuit-level mechanisms whereby continuous increases in the
515 level of hunger cause opposite-direction effects on aggressiveness at different thresholds
516 are likely complex[21,80], and remain to be investigated.

517 Why should the competition between hunger and aggressiveness be reflected by
518 changes in line attractor dynamics? An attractor provides a region of stability in neural
519 state space, to which neural activity rapidly returns if subjected to an off-manifold
520 perturbation[40]. When "hangry" animals engaged in fighting were presented with food
521 pellets, they initially switched from fighting to feeding. Although neural population activity
522 moved out of the attractor during food consumption, activity in the attractor dimension
523 remained elevated. Following such feeding bouts, activity rapidly returned to the line
524 attractor dimension as attack resumed (Fig. 5r). These observations suggest a potential
525 adaptive role for the VMHvl line attractor, namely, to keep hungry animals primed for
526 aggression while feeding in the presence of an intruder. At the manifold level[37,38], we
527 speculate that the "attractive" nature of the integration dimension may provide a
528 counterpoint to the strong motivation to feed, thereby mediating a delicate balance
529 between these competing drives. How this balance is computed and read out to control
530 behavior will be an important question for future investigation.

531 **Acknowledgements**

532 We thank J.S. Chang, X. Da, X. Wang, D. Wagenaar, M. Yee, and L. Salay for technical
533 assistance, K. Lee for mouse care, G. Mountoufaris and K. Cheung for training in
534 miniscope imaging, S.W. Linderman and members of the Anderson laboratory for helpful
535 discussions, L. Chavarria for administrative assistance, and C. Chiu for lab management.
536 This work was supported by NIH grants R01NS123916 and R01MH123612, and the
537 Simons Foundation to D.J.A., a HHMI-HHWF postdoctoral fellowship and postdoc
538 fellowship abroad from the National Research Foundation of Korea (NRF) to J.K., and a
539 National Science Scholarship from the Agency of Science, Technology and Research,
540 Singapore and the Nanyang Assistant Professorship Start-up Grant from Nanyang
541 Technological University, Singapore to A.N. D.J.A. is an Investigator of the Howard
542 Hughes Medical Institute.

543 **Author contribution**

544 J.K. and D.J.A. conceived the project. J.K. performed all experimental work with help from
545 S.H., A.V., and M.L. J.K. and A.N. performed computational analyses. N.C. and A.N.

546 developed data analysis pipelines with help from J.X. J.K., A.N., and D.J.A. analyzed and
547 interpreted the data and co-wrote the manuscript. D.J.A. supervised the project.

548

549 **Competing interests**

550 The authors declare no competing interests.

551 **References**

552 1 Lorenz, K. *On aggression*. 1st edn, (Harcourt, 1966).

553 2 Kennedy, A. *et al.* in *Cold Spring Harbor symposia on quantitative biology.* 199-210
554 (Cold Spring Harbor Laboratory Press).

555 3 Berridge, K. C. Evolving concepts of emotion and motivation. *Frontiers in*
556 *psychology* **9**, 317391 (2018).

557 4 Anderson, D. J. *The nature of the beast: how emotions guide us*. (Basic Books,
558 2022).

559 5 Burnett, C. J. *et al.* Hunger-Driven Motivational State Competition. *Neuron* **92**, 187-
560 201 (2016). https://doi.org/10.1016/j.neuron.2016.08.032

561 6 Burnett, C. J. *et al.* Need-based prioritization of behavior. *Elife* **8**, e44527 (2019).

562 7 Fokidis, H. B., Prior, N. H. & Soma, K. K. Fasting increases aggression and
563 differentially modulates local and systemic steroid levels in male zebra finches.
564 *Endocrinology* **154**, 4328-4339 (2013).

565 8 Nakajo, H. *et al.* Hunger potentiates the habenular winner pathway for social conflict
566 by orexin-promoted biased alternative splicing of the AMPA receptor gene. *Cell*
567 *reports* **31** (2020).

568 9 Edmunds, D., Wigby, S. & Perry, J. C. 'Hangry'Drosophila: food deprivation
569 increases male aggression. *Animal Behaviour* **177**, 183-190 (2021).

570 10 Lim, R. S., Eyjólfsdóttir, E., Shin, E., Perona, P. & Anderson, D. J. How food controls
571 aggression in Drosophila. *PloS one* **9**, e105626 (2014).

572 11 Bushman, B. J., DeWall, C. N., Pond Jr, R. S. & Hanus, M. D. Low glucose relates
573 to greater aggression in married couples. *Proceedings of the National Academy of*
574 *Sciences* **111**, 6254-6257 (2014).

575 12 MacCormack, J. K. & Lindquist, K. A. Feeling hangry? When hunger is
576 conceptualized as emotion. *Emotion* **19**, 301 (2019).

13 Swami, V., Hochstöger, S., Kargl, E. & Stieger, S. Hangry in the field: An experience sampling study on the impact of hunger on anger, irritability, and affect. *Plos one* **17**, e0269629 (2022).

14 Padilla, S. L. *et al.* Agouti-related peptide neural circuits mediate adaptive behaviors in the starved state. *Nature neuroscience* **19**, 734-741 (2016).

15 Rohles, F. H. & Wilson, L. M. Hunger as a catalyst in aggression. *Behaviour* **48**, 123-129 (1974).

16 Lee, H. *et al.* Scalable control of mounting and attack by Esr1+ neurons in the ventromedial hypothalamus. *Nature* **509**, 627-632 (2014).

17 Yang, T. *et al.* Social control of hypothalamus-mediated male aggression. *Neuron* **95**, 955-970. e954 (2017).

18 Yang, C. F. *et al.* Sexually dimorphic neurons in the ventromedial hypothalamus govern mating in both sexes and aggression in males. *Cell* **153**, 896-909 (2013). https://doi.org/10.1016/j.cell.2013.04.017

19 Lin, D. *et al.* Functional identification of an aggression locus in the mouse hypothalamus. *Nature* **470**, 221-226 (2011).

20 Zha, X. & Xu, X. H. Neural circuit mechanisms that govern inter-male attack in mice. *Cell Mol Life Sci* **78**, 7289-7307 (2021). https://doi.org/10.1007/s00018-021-03956-x

21 Lischinsky, J. E. & Lin, D. Neural mechanisms of aggression across species. *Nat Neurosci* **23**, 1317-1328 (2020). https://doi.org/10.1038/s41593-020-00715-2

22 Mei, L., Osakada, T. & Lin, D. Hypothalamic control of innate social behaviors. *Science* **382**, 399-404 (2023).

23 Ingraham, H. A., Herber, C. B. & Krause, W. C. Running the Female Power Grid Across Lifespan Through Brain Estrogen Signaling. *Annu Rev Physiol* **84**, 59-85 (2022). https://doi.org/10.1146/annurev-physiol-061121-035914

24 Krause, W. C. & Ingraham, H. A. Origins and Functions of the Ventrolateral VMH: A Complex Neuronal Cluster Orchestrating Sex Differences in Metabolism and Behavior. *Adv Exp Med Biol* **1043**, 199-213 (2017). https://doi.org/10.1007/978-3-319-70178-3_10

25 Kosse, C., Ivanov, J., Knight, Z., Pellegrino, K. & Friedman, J. A subcortical feeding circuit linking an interoceptive node to jaw movement. *Nature* **636**, 151-161 (2024). https://doi.org/10.1038/s41586-024-08098-1

26 Kim, D.-W. *et al.* Multimodal analysis of cell types in a hypothalamic node controlling social behavior. *Cell* **179**, 713-728. e717 (2019).

27 Knoedler, J. R. *et al.* A functional cellular framework for sex and estrous cycle-dependent gene expression and behavior. *Cell* **185**, 654-671 e622 (2022). https://doi.org/10.1016/j.cell.2021.12.031

28 Liu, M., Kim, D. W., Zeng, H. & Anderson, D. J. Make war not love: The neural substrate underlying a state-dependent switch in female social behavior. *Neuron* **110**, 841-856 e846 (2022). https://doi.org/10.1016/j.neuron.2021.12.002

29 Yin, L. *et al.* VMHvll(Cckar) cells dynamically control female sexual behaviors over the reproductive cycle. *Neuron* **110**, 3000-3017 e3008 (2022). https://doi.org/10.1016/j.neuron.2022.06.026

30 Lo, L. *et al.* Connectional architecture of a mouse hypothalamic circuit node controlling social behavior. *Proc Natl Acad Sci U S A* **116**, 7503-7512 (2019). https://doi.org/10.1073/pnas.1817503116

31 Correa, S. M. *et al.* An estrogen-responsive module in the ventromedial hypothalamus selectively drives sex-specific activity in females. *Cell Rep* **10**, 62-74 (2015). https://doi.org/10.1016/j.celrep.2014.12.011

32 Osakada, T. *et al.* A dedicated hypothalamic oxytocin circuit controls aversive social learning. *bioRxiv*, 2022.2012.2014.519639 (2022). https://doi.org/10.1101/2022.12.14.519639

33 Remedios, R. *et al.* Social behaviour shapes hypothalamic neural ensemble representations of conspecific sex. *Nature* **550**, 388-392 (2017). https://doi.org/10.1038/nature23885

34 Falkner, A. L., Dollar, P., Perona, P., Anderson, D. J. & Lin, D. Decoding ventromedial hypothalamic neural activity during male mouse aggression. *J. Neurosci.* **34**, 5971-5984 (2014). https://doi.org/10.1523/JNEUROSCI.5109-13.2014

35 Ebitz, R. B. & Hayden, B. Y. The population doctrine in cognitive neuroscience. *Neuron* **109**, 3055-3068 (2021). https://doi.org/10.1016/j.neuron.2021.07.011

36 Barack, D. L. & Krakauer, J. W. Two views on the cognitive brain. *Nat Rev Neurosci* **22**, 359-371 (2021). https://doi.org/10.1038/s41583-021-00448-6

37 Langdon, C., Genkin, M. & Engel, T. A. A unifying perspective on neural manifolds and circuits for cognition. *Nat Rev Neurosci* **24**, 363-377 (2023). https://doi.org/10.1038/s41583-023-00693-x

38 Perich, M. G., Narain, D. & Gallego, J. A. A neural manifold view of the brain. *Nat Neurosci* (2025). https://doi.org/10.1038/s41593-025-02031-z

39 Vyas, S., Golub, M. D., Sussillo, D. & Shenoy, K. V. Computation Through Neural Population Dynamics. *Annu Rev Neurosci* **43**, 249-275 (2020). https://doi.org/10.1146/annurev-neuro-092619-094115

40 Khona, M. & Fiete, I. R. Attractor and integrator networks in the brain. *Nat Rev Neurosci* **23**, 744-766 (2022). https://doi.org/10.1038/s41583-022-00642-0

41 Hulse, B. K. & Jayaraman, V. Mechanisms Underlying the Neural Computation of Head Direction. *Annu Rev Neurosci* **43**, 31-54 (2020). https://doi.org/10.1146/annurev-neuro-072116-031516

42 Mante, V., Sussillo, D., Shenoy, K. V. & Newsome, W. T. Context-dependent computation by recurrent dynamics in prefrontal cortex. *Nature* **503**, 78-84 (2013). https://doi.org/10.1038/nature12742

43 Sylwestrak, E. L. *et al.* Cell-type-specific population dynamics of diverse reward computations. *Cell* **185**, 3568-3587 e3527 (2022). https://doi.org/10.1016/j.cell.2022.08.019

44 Inagaki, H. K., Fontolan, L., Romani, S. & Svoboda, K. Discrete attractor dynamics underlies persistent activity in the frontal cortex. *Nature* **566**, 212-217 (2019). https://doi.org/10.1038/s41586-019-0919-7

45 Seung, H. S. How the brain keeps the eyes still. *Proceedings of the National Academy of Sciences* **93**, 13339-13344 (1996).

46 Nair, A. *et al.* An approximate line attractor in the hypothalamus encodes an aggressive state. *Cell* **186**, 178-193. e115 (2023).

47 Vinograd, A., Nair, A., Kim, J. H., Linderman, S. W. & Anderson, D. J. Causal evidence of a line attractor encoding an affective state. *Nature* **634**, 910-918 (2024).

48 Mountoufaris, G. *et al.* A line attractor encoding a persistent internal state requires neuropeptide signaling. *Cell* **187**, 5998-6015. e5918 (2024).

49 Flavell, S. W., Gogolla, N., Lovett-Barron, M. & Zelikowsky, M. The emergence and influence of internal states. *Neuron* **110**, 2545-2570 (2022).

50 Encarnacion-Rivera, L., Deisseroth, K. & Luo, L. Neurobiology of Thirst and Hunger Drives. *Annu Rev Neurosci* (2025). https://doi.org/10.1146/annurev-neuro-112723-032328

51 Richman, E. B., Ticea, N., Allen, W. E., Deisseroth, K. & Luo, L. Neural landscape diffusion resolves conflicts between needs across time. *Nature* **623**, 571-579 (2023). https://doi.org/10.1038/s41586-023-06715-z

52 Krashes, M. J. *et al.* Rapid, reversible activation of AgRP neurons drives feeding behavior in mice. *J Clin Invest* **121**, 1424-1428 (2011). https://doi.org/10.1172/JCI46229

53 Aponte, Y., Atasoy, D. & Sternson, S. M. AGRP neurons are sufficient to orchestrate feeding behavior rapidly and without training. *Nat Neurosci* **14**, 351-355 (2011). https://doi.org/10.1038/nn.2739

54 Sternson, S. M. & Eiselt, A. K. Three Pillars for the Neural Control of Appetite. *Annu Rev Physiol* **79**, 401-423 (2017). https://doi.org/10.1146/annurev-physiol-021115-104948

55 Karigo, T. *et al.* Distinct hypothalamic control of same- and opposite-sex mounting behaviour in mice. *Nature* **589**, 258-263 (2021). https://doi.org/10.1038/s41586-020-2995-0

56 Datta, S. R., Anderson, D. J., Branson, K., Perona, P. & Leifer, A. Computational Neuroethology: A Call to Action. *Neuron* **104**, 11-24 (2019). https://doi.org/10.1016/j.neuron.2019.09.038

57 Segalin, C. *et al.* The Mouse Action Recognition System (MARS) software pipeline for automated analysis of social behaviors in mice. *Elife* **10**, e63720 (2021).

58 Ziv, Y. *et al.* Long-term dynamics of CA1 hippocampal place codes. *Nat Neurosci* **16**, 264-266 (2013). https://doi.org/10.1038/nn.3329

59 Liu, M., Nair, A., Coria, N., Linderman, S. W. & Anderson, D. J. Encoding of female mating dynamics by a hypothalamic line attractor. *Nature* **634**, 901-909 (2024).

60 Weissbourd, B. *et al.* A genetically tractable jellyfish model for systems and evolutionary neuroscience. *Cell* **184**, 5854-5868 e5820 (2021). https://doi.org/10.1016/j.cell.2021.10.021

61 Pillow, J. W. *et al.* Spatio-temporal correlations and visual signalling in a complete neuronal population. *Nature* **454**, 995-999 (2008). https://doi.org/10.1038/nature07140

62 Major, G. & Tank, D. Persistent neural activity: prevalence and mechanisms. *Curr Opin Neurobiol* **14**, 675-684 (2004). https://doi.org/10.1016/j.conb.2004.10.017

63 Cavanagh, S. E., Towers, J. P., Wallis, J. D., Hunt, L. T. & Kennerley, S. W. Reconciling persistent and dynamic hypotheses of working memory coding in prefrontal cortex. *Nat Commun* **9**, 3498 (2018). https://doi.org/10.1038/s41467-018-05873-3

64 Murray, J. D. *et al.* A hierarchy of intrinsic timescales across primate cortex. *Nat Neurosci* **17**, 1661-1663 (2014). https://doi.org/10.1038/nn.3862

65 Linderman, S. W. *et al.* Recurrent switching linear dynamical systems. *arXiv preprint arXiv:1610.08466* (2016).

66 Glaser, J., Whiteway, M., Cunningham, J. P., Paninski, L. & Linderman, S. 14867-14878 (Curran Associates, Inc.).

67 Alcantara, I. C., Tapia, A. P. M., Aponte, Y. & Krashes, M. J. Acts of appetite: neural circuits governing the appetitive, consummatory, and terminating phases of feeding. *Nat Metab* **4**, 836-847 (2022). https://doi.org/10.1038/s42255-022-00611-y

68 Su, Z., Alhadeff, A. L. & Betley, J. N. Nutritive, Post-ingestive Signals Are the Primary Regulators of AgRP Neuron Activity. *Cell Rep* **21**, 2724-2736 (2017). https://doi.org/10.1016/j.celrep.2017.11.036

69 Nakajima, K. *et al.* Corrigendum: Gs-coupled GPCR signalling in AgRP neurons triggers sustained increase in food intake. *Nat Commun* **7**, 11019 (2016). https://doi.org/10.1038/ncomms11019

70 Nagai, Y. *et al.* Deschloroclozapine, a potent and selective chemogenetic actuator enables rapid neuronal and behavioral modulations in mice and monkeys. *Nat Neurosci* **23**, 1157-1167 (2020). https://doi.org/10.1038/s41593-020-0661-3

71 Georgiev, A. V., Klimczuk, A. C., Traficonte, D. M. & Maestripieri, D. When violence pays: a cost-benefit analysis of aggressive behavior in animals and humans. *Evol Psychol* **11**, 678-699 (2013). https://doi.org/10.1177/147470491301100313

72 Yang, T. & Shah, N. M. Molecular and neural control of sexually dimorphic social behaviors. *Curr Opin Neurobiol* **38**, 89-95 (2016). https://doi.org/10.1016/j.conb.2016.04.015

73 Tu, L., Fukuda, M., Tong, Q. & Xu, Y. The ventromedial hypothalamic nucleus: watchdog of whole-body glucose homeostasis. *Cell Biosci* **12**, 71 (2022). https://doi.org/10.1186/s13578-022-00799-2

74 Hirschberg, P. R., Sarkar, P., Teegala, S. B. & Routh, V. H. Ventromedial hypothalamus glucose-inhibited neurones: A role in glucose and energy homeostasis? *J Neuroendocrinol* **32**, e12773 (2020). https://doi.org/10.1111/jne.12773

75 Adolphs, R. & Anderson, D. J. *The Neuroscience of Emotion: A New Synthesis*. (Princeton University Press, 2018).

76 Sutton Hickey, A. K. & Krashes, M. J. Integrating Hunger with Rival Motivations. *Trends Endocrinol Metab* **31**, 495-507 (2020). https://doi.org/10.1016/j.tem.2020.04.006

77 Malezieux, M., Klein, A. S. & Gogolla, N. Neural Circuits for Emotion. *Annu Rev Neurosci* **46**, 211-231 (2023). https://doi.org/10.1146/annurev-neuro-111020-103314

78 Betley, J. N. *et al.* Neurons for hunger and thirst transmit a negative-valence teaching signal. *Nature* **521**, 180-185 (2015). https://doi.org/10.1038/nature14416

79 Charnov, E. L. Optimal foraging, the marginal value theorem. *Theor Popul Biol* **9**, 129-136 (1976). https://doi.org/10.1016/0040-5809(76)90040-x

80 de Araujo Salgado, I. *et al.* Toggling between food-seeking and self-preservation behaviors via hypothalamic response networks. *Neuron* **111**, 2899-2917 e2896 (2023). https://doi.org/10.1016/j.neuron.2023.06.006

81 Hong, W. *et al.* Automated measurement of mouse social behaviors using depth sensing, video tracking, and machine learning. *Proc Natl Acad Sci U S A* **112**, E5351-5360 (2015). https://doi.org/10.1073/pnas.1515982112

82 Yang, B., Karigo, T. & Anderson, D. J. Transformations of neural representations in a social behaviour network. *Nature* **608**, 741-749 (2022). https://doi.org/10.1038/s41586-022-05057-6

83 Zhou, P. *et al.* Efficient and accurate extraction of in vivo calcium signals from microendoscopic video data. *Elife* **7** (2018). https://doi.org/10.7554/eLife.28728

84 Shadlen, M. N., Britten, K. H., Newsome, W. T. & Movshon, J. A. A computational analysis of the relationship between neuronal and behavioral responses to visual motion. *J Neurosci* **16**, 1486-1510 (1996). https://doi.org/10.1523/JNEUROSCI.16-04-01486.1996

780 **METHODS**

781 **Animals**

782 All experimental procedures involving the use of live mice or their tissues were carried
783 out following NIH guidelines and approved by the Institute Animal Care and Use
784 Committee (IACUC) and the Institute Biosafety Committee (IBC) at the California Institute
785 of Technology (Caltech). All mice in this study, including wild-type and transgenic mice,
786 were bred at Caltech or purchased from Charles River Laboratory. Group housed
787 C57BL/6N female or singly housed male mice (2-5 months) were used as experimental
788 mice. *Esr1*^{cre} mice, *Esr1*^{flp} mice were backcrossed into the C57BL/6N background (>N10)
789 and bred at Caltech. Heterozygous *Esr1*^{cre} or double heterozygote *Esr1*$^{flp/+}$*AgRP*$^{cre/+}$ mice
790 were used for cell-specific targeting experiments and were genotyped by PCR analysis
791 using genomic DNA from tail tissue. All mice were housed in ventilated micro-isolator
792 cages in a temperature-controlled environment (median temperature 23°C, humidity
793 60%), under a reversed 11-h dark–13-h light cycle, with *ad libitum* access to food and
794 water. Mouse cages were changed weekly.

795 **Housing conditions for social and sexual experience**

796 All male C57BL/6N mice used in this study were socially and sexually experienced. Mice
797 aged 8–12 weeks were initially co-housed with a female BALB/c mouse for 1 week and
798 were screened for male-typical social behaviors. Mice that showed both mounting
799 towards females and attacking towards males during a 30-minute resident intruder assay
800 were selected for surgery and subsequent behavior experiments. From this point forward,
801 these male mice were always co-housed with non-pregnant female BALB/c mice.

802 **Stereotaxic Surgeries**

803 Virus injection and implantation were performed as described previously[33,37]. Briefly,
804 animals were anesthetized with isoflurane (5% for induction and 1.5% for maintenance)
805 and placed on a stereotaxic frame (David Kopf Instruments). The virus was injected into
806 the target area using a pulled-glass capillary (World Precision Instruments) and a
807 pressure injector (Micro4 controller, World Precision Instruments), at a 20 nl min^{-1} flow

808 rate. The glass capillary was left in place for ten minutes following injection before
809 withdrawal. Integrated GRIN Lenses (Inscopix) were slowly lowered into the brain and
810 fixed to the skull with dental cement (Metabond, Parkell). After virus injection and lens
811 implantation, males were co-housed with an ovariectomized or non-pregnant female
812 mouse. Four to six weeks after lens implantation, mice were head-fixed on a running
813 wheel, and a miniaturized micro-endoscope (nVista, Inscopix) was lowered over the
814 implanted lens until GCaMP-expressing fluorescent neurons were in focus.

815 **Virus injection and GRIN lens implantation**

816 The following AAVs were used in this study, with injection titers as indicated. Viruses with
817 a high original titer were diluted with clean PBS on the day of use. AAV1-EF1a-FLEX-
818 GCaMP8m (~2.3 x10^{12}vg/ml, Addgene), AAVdj-hSyn-fDIO-GCaMP8m (~2.0x10^{12} vg/ml,
819 Janelia Vector Core), and AAV8-DIO-hM3Dq (4x10^{12} vg/ml, Addgene).

820 **Stereotaxic coordinates for the viral injection (unless specified):**
821 VMHvl, AP: −1.6, ML: ±0.78, DV: −5.7 (from the skull surface)
822 ARC, AP: -1.7, ML: ±0.25, DV: -5.85 mm (from the bregma)
823 Stereotaxic injection coordinates were based on the Paxinos and Franklin atlas. GRIN
824 lens implantation: VMHvl, AP: −1.6, ML: −0.76, DV: −5.55 (⌀0.6 × 7.3 mm GRIN lens).

825 **Behavioral assays**

826 Prior to resident-intruder (RI) assays, male mice were co-housed with females to have
827 sexual experience for at least one week. Before the assay, cohoused females were
828 removed from the home cage for at least two days. Male mice were acclimated to the
829 behavioral room with a dimmed red light for two consecutive days, followed by a third day
830 of habituation for five minutes of interaction with a male Balb/c mouse to reduce any
831 novelty. The day before the RI assay, mice were separated into 'fed' or 'fasted' cohorts,
832 counter-balanced for the order of conditions. At the onset of fasting (food removal), every
833 mouse in the relevant cohort was singly transferred into a new home cage with fresh
834 bedding. On the day of the RI assay, mice were habituated to the behavior chamber for
835 10 minutes, followed by a 'baseline' for 5 minutes. A novel Balb/c male (or for mating
836 assays, a sexually experienced/hormonally primed female mouse) was introduced, and

837 the RI session continued for 5 or 10 minutes. For the choice assay, following an initial 2
838 min interaction with a male intruder either a 2.5-4g normal chow pellet (or, as a control,
839 the cap of a 15ml Falcon tube) was dropped into the home cage, leaving the intruder in
840 place. After two minutes of observation, the intruder was removed and the test mouse left
841 alone with the food pellet for an additional 5-10 minutes to assess its feeding behavior.

842 **Behavior recording**

843 All behavioral experiments were performed in conventional mouse housing cages (the
844 resident mouse's home cage) under red lighting, using the previously described behavior
845 recording setup [81]. The behavior video's top and front views were acquired at 30 Hz using
846 StreamPix9 (Norpix) video recording software.

847 **Behavior Annotations**

848 Behavior videos (top and side views) were manually annotated using a custom MATLAB-
849 based behavioral annotation interface called BENTO[57].

850 We manually annotated the following resident male behaviors:

851 During male-male interactions: sniffing the male (body, genital, and face), dominance
852 mounting, and attack. For analysis of the imaging experiment, we also detailed the
853 intruders' behaviors, including exploration of the cage, immobility, and defensive postures
854 (exposing their abdominal parts while standing). During male-female interactions, sniffing
855 the female (body, genitals, and face), mounting, and intromission were scored. During
856 male-food interaction, sniffing food and eating were scored.

857 **Chemogenetic activation**

858 Behavioural tests were performed at three day intervals, at minimum. The order and
859 number of mice receiving saline or DCZ (Sigma) were counterbalanced across different
860 conditions. DCZ was dissolved in DMSO and further diluted in saline; DCZ (0.1, 0.5,
861 1.0 mg/kg of body weight) or saline (control) was intraperitoneally (i.p.) injected 40-50 min
862 before behavioral tests.

863

Chemoscope imaging

For experiments combining miniscope imaging with chemogenetic manipulations ("Chemoscope"[82]), to minimize population activity changes associated with stress from i.p. injections, a series of habituation sessions was performed every two consecutive days before any test conditions used for analysis. Mice were injected with 10ul/g (body weight) of saline (control) and returned to their home cage for 40-50 min before imaging[82]. On the test day, mice were injected with control or 10ul/g of different doses of DCZ (0.5 vs 1.0mg/kg). The order and number of mice in each condition were randomized, and other conditions were performed at 2-3 days intervals. On the day of imaging, mice were injected 40-50 mins before the RI assay.

Miniscope data acquisition and extraction

On the day of imaging, mice were habituated for at least 10 minutes after installing the miniscope (Bruker, Inc.) in their home cage before the start of the behavior tests. Imaging data were acquired at 30 Hz with spatial down sampling (2); light-emitting diode power (0.2) and gain (3–6) were adjusted depending on the brightness of GCaMP expression as determined by the image histogram according to the user manual. A transistor–transistor logic (TTL) pulse from the Sync port of the data acquisition box (DAQ, Inscopix) was used for synchronous triggering of StreamPix9 (Norpix) for video recording. Imaging sessions typically lasted 30 mins per day. Preprocessing and motion correction were performed using Inscopix Data Processing Software. Briefly, the raw imaging data were spatially sampled twice, motion corrected, and temporally downsampled to 10 Hz, and then exported as a .tiff image stack. A spatial band-pass filter was then applied to remove the out-of-focus background. After preprocessing, calcium traces were extracted and deconvolved using the CNMF-E large data pipeline[83] with the following parameters: patch_dims = [32, 32], gSig = 3, gSiz = 13, ring_radius = 15, min_corr = 0.7-0.8, min_pnr = 8. Every extracted unit's spatial and temporal components were carefully inspected manually (signal-to-noise ratio, peak-to-noise ratio, size, motion artifacts, decay kinetics, and so on), and outliers (apparent deviations from the normal distribution) were discarded. The extracted traces were then z-scored before further analysis.

894

895 **Longitudinal imaging data extraction and preprocessing**

896 We imaged the male mice implanted with a GRIN lens for multiple days under varying
897 durations of food deprivation in a non-consecutive manner with two to three days' intervals.
898 On the day of imaging, we compared the field of view with a reference mark to ensure the
899 accuracy of registration of the spatial FOV across different days. Miniscope data was
900 selected and concatenated into one .isxd file. Data was preprocessed, and the traces
901 were extracted as described in the last section. The extracted traces were z-scored and
902 split into multiple traces for individual days[59]. If two imaging sessions were compared
903 directly, the cell registration algorithm[83] in the CIAtah was used to extract traces in the
904 registered cells.

905 **Immunohistochemistry**

906 For Fig.4a, animals were anesthetized with isoflurane 90 mins after 1 mg/kg DCZ
907 treatment and cordially perfused with 30 ml of cold 4% PFA following 30 ml of 0.9% saline.
908 Brains were post-fixated for 4 hrs in 4% PFA at 4°C and then transferred to 30% sucrose
909 in PBS. Brains were coronally sectioned at 60 μm using a Leica cryostat. The sectioned
910 brains were washed with PBS for 10 mins and blocked with 2 % normal donkey serum in
911 0.2% PBST for 1 hr at R.T. Primary antibodies, goat anti-cFos (1:200, Santa Cruz, sc 52-
912 g), mouse anti-NPY (1:1000, Santa Cruz, sc-133080), in the blocking solution (2% NDS
913 in 0.2% PBST-Triton X-100) were incubated at 4°C for 72 hours. The sections were
914 washed with PBS (3 x 15 mins), followed by incubation of the second antibody, donkey
915 anti-mouse Alexa 647 (1:500, Life Technologies, A21207) or donkey anti-goat Alexa 488
916 (1:500, Life Technologies, A11055), for 1 hr at RT. Then they were washed with PBS (2 x
917 15 mins), stained with DAPI (1:10000) for 6 mins, and mounted with DAKO mounting
918 medium. Confocal images were captured with an Olympus microscope.

919 **Data Analysis |**

920 **Calculation of pixel changes and pose estimation using MARS**

Pose estimation was performed using MARS[57] to identify specific body parts ("keypoints") of the resident mouse and the intruder mouse during behavioral assays. After identifying keypoints, pixel changes were computed to quantify pose dynamics during behavior bouts, such as sniffing or attack. Specifically, pixel change was calculated within a defined region—a square measuring 20x20 pixels—surrounding each identified keypoint on the resident mouse. This calculation was performed on a frame-by-frame basis throughout the duration of each bout of sniffing or attack behavior. This metric of pixel change thus provides a quantitative measure of pose dynamics and movement intensity localized to each relevant body part, allowing comparisons of these parameters between fed and fasted conditions.

Choice Probability (CP)

Choice probability (CP) analysis was performed as previously described[33,55] to quantify a neuron's selectivity or "tuning," defined here as the ability to discriminate between two behavioral conditions based on single-cell activity[84]. For each neuron, the CP was calculated by constructing histograms of its $\Delta F(t)/F0$ activity values during the two conditions of interest. These histograms were compared to generate a receiver operating characteristic (ROC) curve, from which CP was determined by calculating the integral of the area under the curve (AUC). CP values range from 0 to 1, with 0.5 representing chance-level discrimination. To assess statistical significance, we performed a shuffle-based permutation test by randomizing the timing of behavioral events across the two conditions and recalculating CP 100 times. Observed CP values were considered significant if they exceeded two standard deviations (2σ) above the mean shuffled CP distribution and additionally surpassed an absolute CP threshold of 0.75, consistent with established criteria[33,55]. Colored bars indicate neurons exhibiting robust and statistically significant CP values, whereas grey bars represent neurons whose CP either fell below the 2σ significance threshold or failed to exceed the established CP criterion of 0.75.

Generalized linear model (GLM)

To predict neural activity from behavior, we trained generalized linear models to predict the activity of each neuron k, as a weighted linear combination of male-directed

behaviors (male sniffing and attack behaviors) or food-directed behaviors (food sniffing and eating behaviors), as follows:

$$y_k(t)=\vec{x}(t)\vec{\beta}+\varphi$$

Here, $y_k(t)$ is the calcium activity of neuron k at time t, $\vec{x}(t)$ is a feature vector of 3 binary male behaviors at time lags ranging from t-D to t where D = 10s. $\vec{\beta}$ is a behavior filter that describes how a neuron integrates stimulus over a 10s period. φ is an error term. The model was fit using 10-fold cross-validation with ridge regularization, and model performance is reported as cross-validated R^2 (cvR^2). To account for cell-cell interactions within the network, we also used the activity of simultaneously imaged neurons as regressors in addition to behavior, as previously described[59].

Dynamical system models of neural data

rSLDS models fit the neural data as previously described[46]. In brief, rSLDS is a generative state-space model that decomposes nonlinear time-varying data into discrete states, each with simple linear dynamics. The model describes three sets of variables: discrete states (z) and latent factors (x) that represent the low-dimensional features from the population activity of recorded neurons (y). While the model can also allow for the incorporation of inputs based on behavior features, such external inputs were not included in the first analysis.

The model is formulated as follows: At each time point, there is a discrete state $z_t \in [1, \dots, K]$ that depends recurrently on the continuous latent factors (x) as follows:

$$p(z_{t+1} \mid z_t = k, x_t) = \mathrm{softmax}\{R_k x_t + r_k\} \quad (1)$$

where $R_k \in \mathbb{R}^{K\times K}$ and $r_k \in \mathbb{R}^K$ parameterizes a map from the previous discrete state and continuous state to a distribution over the following discrete states using a softmax link function. The discrete statez_t determines the linear dynamical system used to generate the latent factors at any time t:

$$x_t = A_{z_t} x_{t-1} + b_{z_t} + \epsilon_t \quad (2)$$

where $A_k \in \mathbb{R}^{d \times d}$ is a dynamics matrix and $b_k \in \mathbb{R}^D$ is a bias vector, where D is the dimensionality of the latent space and $\epsilon_t \sim N(0, Q_{z_t})$ is a Gaussian-distributed noise (aka innovation) term where $Q_{z_t} \in \mathbb{R}^{D \times D}$.

Lastly, we can recover the activity of recorded neurons by modeling activity as a linear, noisy Gaussian observation$y_t \in \mathbb{R}^N$ where *N* is the number of recorded neurons:

$$y_t = Cx_t + d + \delta_t \tag{3}$$

For $C \in \mathbb{R}^{N \times D}$ and $\delta_t \sim N(0, S)$, a Gaussian noise term. Overall, the system parameters that rSLDS needs to learn consist of the state transition dynamics, the library of linear dynamical system matrices, and the neuron-specific emission parameters, which we write as:

$$\theta = [(A_k b_k, Q_k, R_k, r_k)_{k=1}^{K},\ C, d, S] \tag{4}$$

We evaluate model performance using both the evidence lower bound (ELBO) and the forward simulation accuracy (FSA) previously described[46] and by calculating the variance explained by the model on the data. Briefly, given observed neural activity in the reduced neural state space at time t, we predict the trajectory of population activity over an ensuing short time interval Δt using the fit rSLDS model, then compute the mean squared error (MSE) between that trajectory and the observed data at time t+ Δt. This MSE is computed across all dimensions of the reduced latent space and repeated across cross-validation folds. This error metric is normalized to a 0-1 range in each animal across the holding to obtain a bounded measure of model performance. The FSA can intuit where model performance drops during the recording. In addition to MSE, we also calculate the Pearson's correlation coefficient (R^2) between the predicted and observed data for each dimension following the forward simulation. By taking the average correlation coefficient across dimensions, we can obtain a quantitative estimate of variance explained by rSLDS on observed data.

The number of states and dimensions used for the model is determined using 5-fold cross-validation. Visualization of the dynamical system using principal components analysis is performed as described previously[46].

Code used to fit rSLDS on neural data is available in the SSM package: (https://github.com/lindermanlab/ssm)

Estimation of time constants

We estimated the time constant of each dimension of linear dynamical systems using eigenvalues λ_a of the dynamics matrix of that system, derived previously[40] as:

$$\tau_a = \left|\frac{1}{\log(|\lambda_a|)}\right| \tag{5}$$

Calculation of line attractor stability

As a quantitative measure to estimate the variance of approximate line-attractor dynamics, we calculated a log 2 ratio between time constants from X_1 and X_2 dimensions as previously defined (sometimes referred to as the "line attractor score")[46-48,59] as:

$$log_2 \frac{t_n}{t_{n-1}}$$

where t_n and t_{n-1} are the first and second largest time constants of the dynamics matrix.

Correlation of time-to-peak of integration dimension and latency to first attack

We estimated the linear correlation between the time to peak of the integration dimension or the time to initiate the first attack behavioral action from the time of initiation of sniffing the intruder.

Calculation of auto-correlation half-width

We computed autocorrelation half-widths by calculating the autocorrelation function for each neuron's time series data (y_t) for a set of lags as described previously[22]. Briefly, for a time series (y_t), the autocorrelation for lag k is:

$$r_k = \frac{c_k}{c_0}$$

where c_k is defined as:

$$c_k = \frac{1}{T}\sum_{t=1}^{T-k}(y_t - \bar{y})(y_{t+k} - \bar{y})$$

and c_0 is the sample variance of the data. The half-width is found for each neuron as the point where the autocorrelation function reaches a value of 0.5.

Decoding of behaviors from the rSLDS dimensions

To evaluate whether the integration dimension (X_1) or X_3 dimensions could discriminate between attack and eating behaviors, we trained a frame-wise decoder as previously described [46,55]. Briefly, behavioral "trials" were constructed by concatenating behavioral bouts separated by less than five seconds. We then trained a linear support vector machine (SVM) classifier to determine an optimal decoding threshold for distinguishing the normalized integration dimension signal[46] during frames associated with attack versus eating behaviors. For shuffled control data, behavioral annotations were randomized across bouts within each trial to disrupt genuine correlations, with this shuffling procedure repeated 20 times per intruder and per mouse. Decoder performance was quantified using the F1 score, averaged across held out "trials" for each animal. Additionally, to rigorously control for potential artifacts arising from slow decay dynamics in the integration dimension, we implemented a permutation test inspired by previous studies[46]. Specifically, a decoding threshold obtained from one mouse was applied to the integration dimension data of all other mice. High performance under this cross-animal decoding paradigm would indicate that decoding accuracy reflects robust behavioral discriminability rather than spurious correlations due to slow drifts in neural activity.

Quantification and statistical analysis

All statistical analyses were performed with GraphPad Prism 9.0.2. We conducted unpaired two-tailed t-tests to compare two groups that present the normal distribution. In the experiments with paired samples, we used the Wilcoxon matched-pairs signed test or paired t-test. In the experiments with non-paired samples, we used the Mann–Whitney

U test. For multiple comparisons between the groups representing the normal distribution, one-way ANOVAs followed by Holm Sidak's post hoc test were performed. The data are presented as the mean ± SEM. One-way or two-way ANOVA tests were followed by Holm Sidak's post hoc test. The significance threshold was held at a = 0.05, two-tailed (not significant (ns), $p>0.05$; *$p<0.05$; **$p<0.01$; ***$p<0.001$; ****$p<0.0001$.

Reporting summary

Further information on research design is available in the Nature Research Reporting Summary.

Data Availability

The data used in this study are available at the following URLs: (TBN on acceptance).

Code Availability

Code for analysis can be found at https://github.com/lindermanlab/ssm. The supporting analysis code will be made available in DANDI upon publication.

Fig. 1 Moderate food deprivation enhances territorial aggression in male mice

Territorial aggressive behaviors during male-male interaction under fed vs. 18-hr fasted states

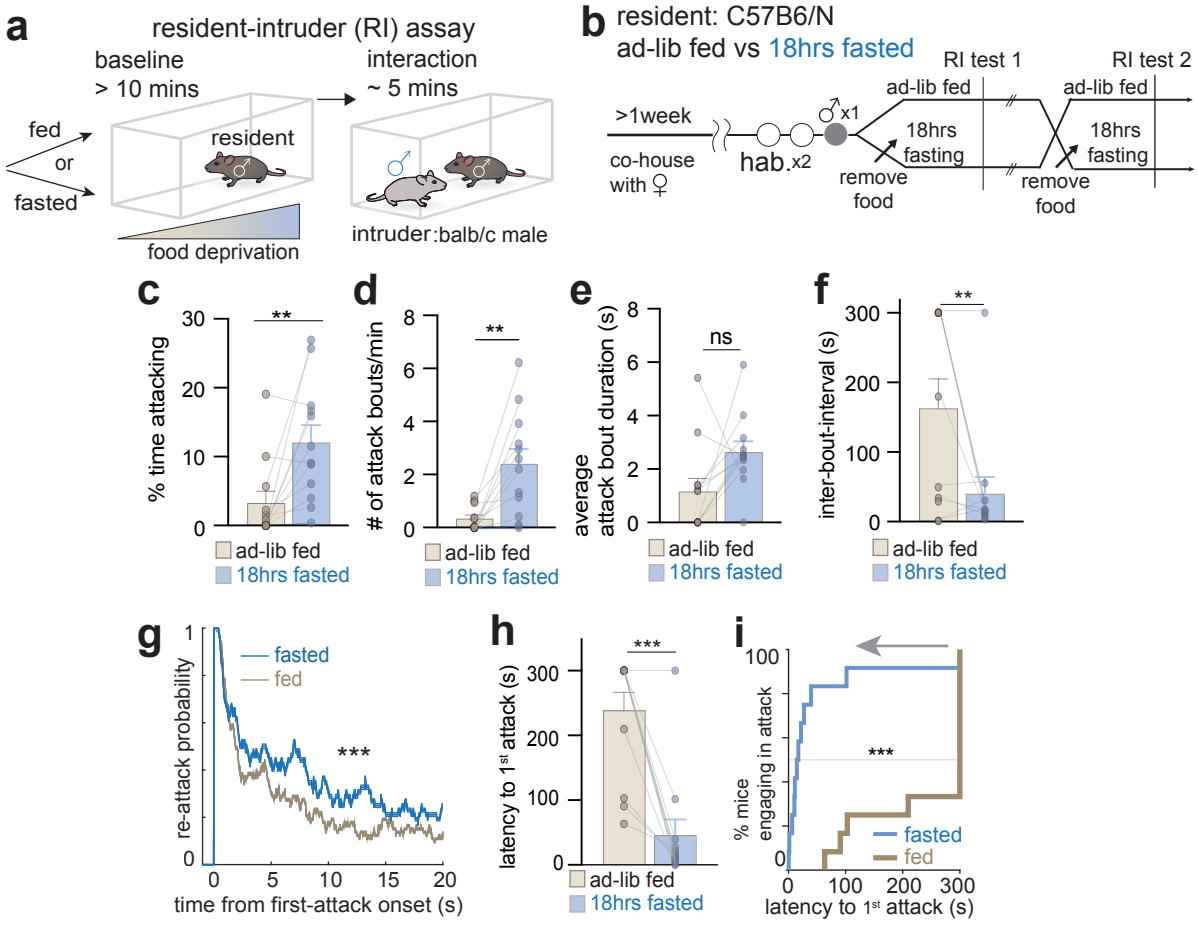

Increase in aggressive behaviors captured by pose estimation in 18 hr fasted states compared to *ad-lib* fed control

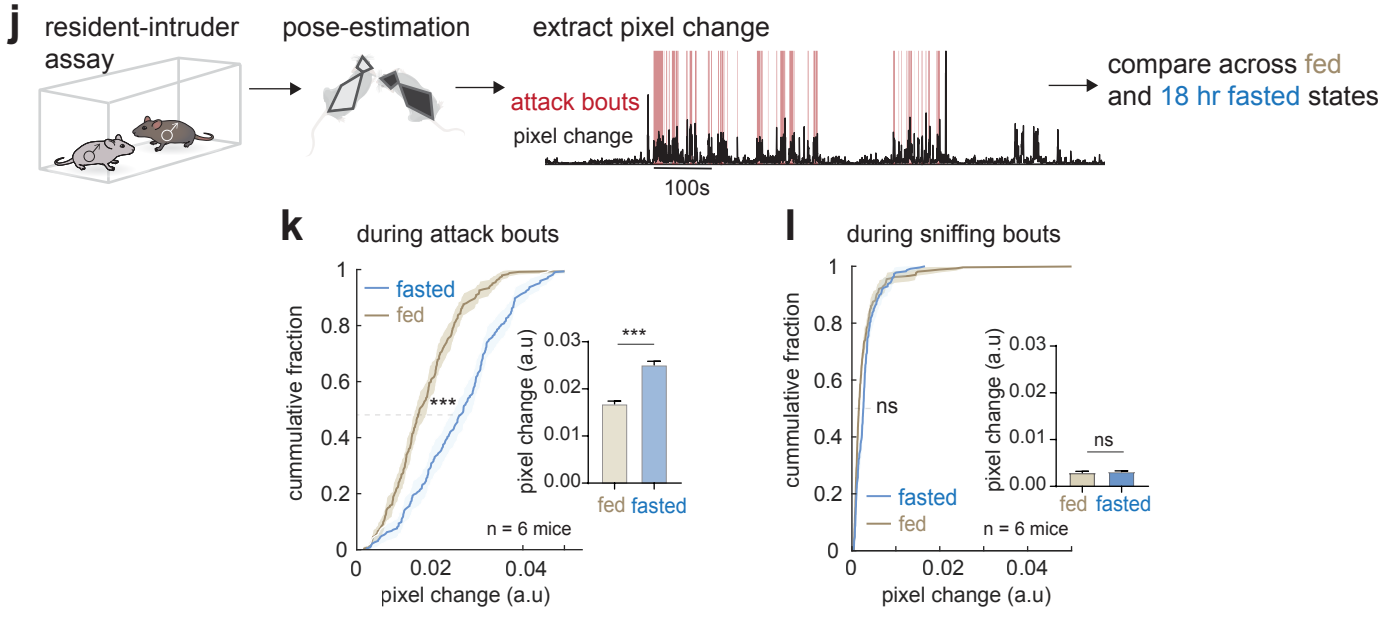

Fig. 1 | Moderate food deprivation enhances aggression in male mice.

(**a**) Schematic of resident-intruder (RI) assay for male-male interactions following *ad libitum*-fed or 18-hr fasting of the resident.

(**b**) Schematic of behavioral paradigm to compare aggressive behaviors across different energy states. The order of fed vs. fasted states was counter-balanced across cohorts, with a 2-day interval between conditions (Methods).

(**c-f, h**) Quantification of aggression parameters: (**c**) time spent in attack (%); (**d**) number of attack bouts/min; (**e**) average attack duration; (**f**) inter-bout-interval; and (**h**) latency to the first attack.

(**g**) Cumulative probability of re-attack after the onset of the first attack bout, across animals (n = 12 mice).

(**i**) Empirical cumulative distribution function (ECDF) plot showing latency to the first attack across the *ad libitum*-fed (brown) vs 18-hr fasted state (blue). Data scaled to 100%.

(**j**) Schematic illustrating unsupervised analysis of pose estimation features (Methods). The pixel change value associated with the resident mouse during each behavioral bout was computed for each mouse and compared across fed vs 18-hr fasted conditions.

(**k-l**) ECDF plots for pixel changes across fed vs. 18-hr fasted states during attack bouts (**k**), and during sniffing bouts (**l**). Bar graphs quantifying the mean pixel change across energy state from 6 mice (right).

$p<0.01$, ***$p<0.001$; ns, not significant. For all figure panels, data are mean ± SEM (n=6 mice in this and all figures unless otherwise indicated). See also **Extended Data Fig. 1.

Fig. 2 Moderate fasting enhances ramping and persistence in a VMHvl^{Esr1} latent slow mode

Longitudinal imaging of VMHvl^{Esr1} neurons

VMHvl^{Esr1} neural activity with male intruder

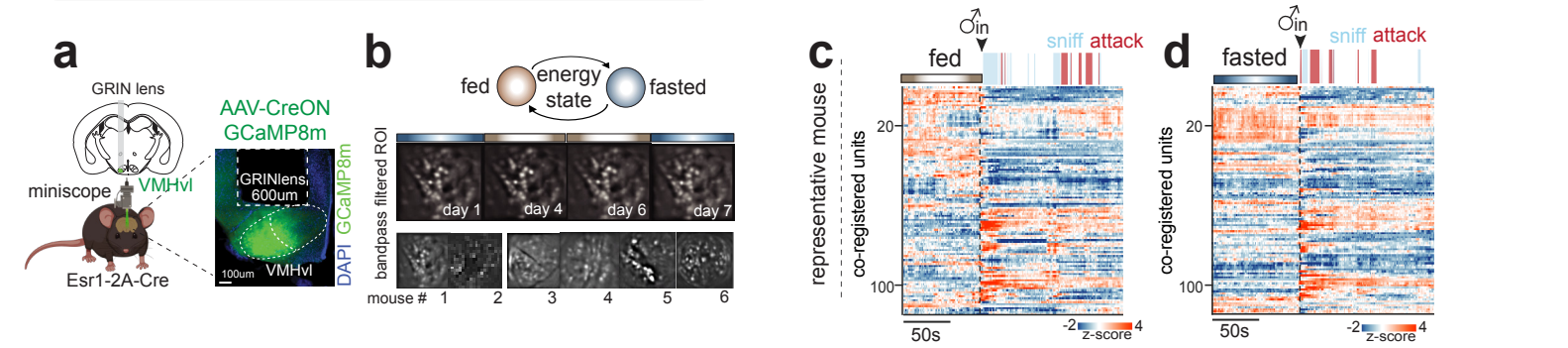

Population dynamics of aggressive state-encoding VMHvl^{Esr1} neurons under fed vs. 18 hr fasted states

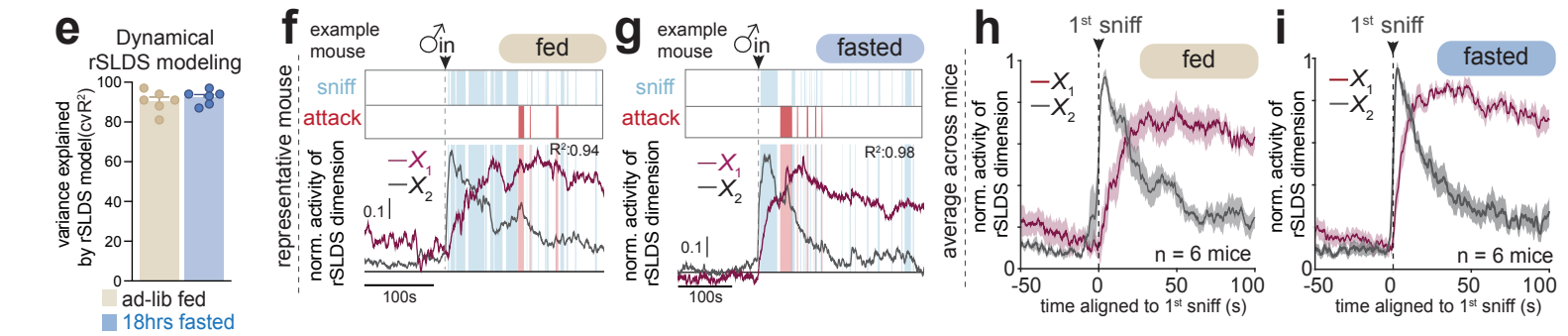

Steeper ramping of VMHvl^{Esr1} population dynamics is correlated with shorter latency to attack in 18 hr fasted state

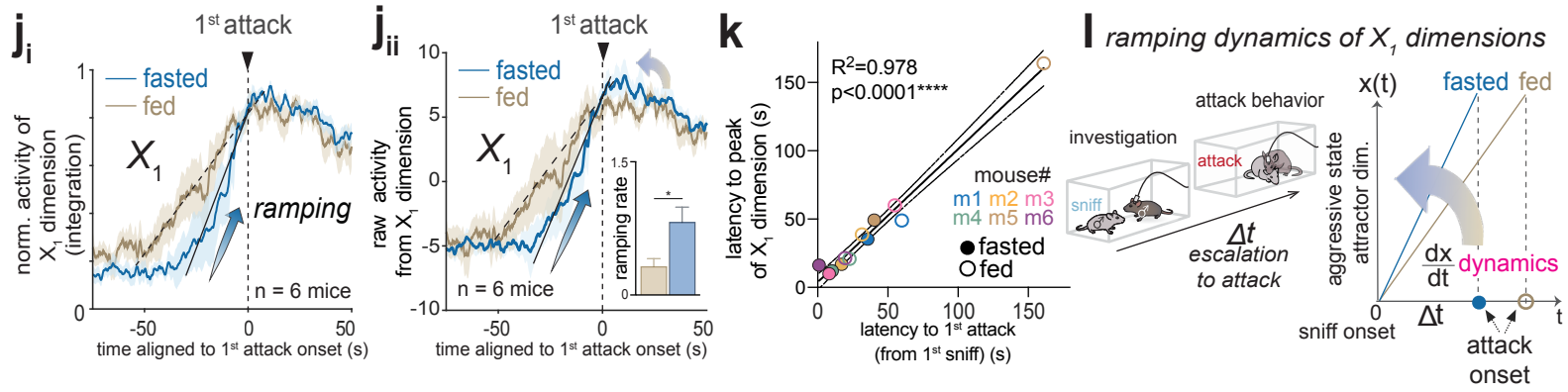

Stability of VMHvl^{Esr1} neural population dynamics under fed vs. 18 hr fasted states

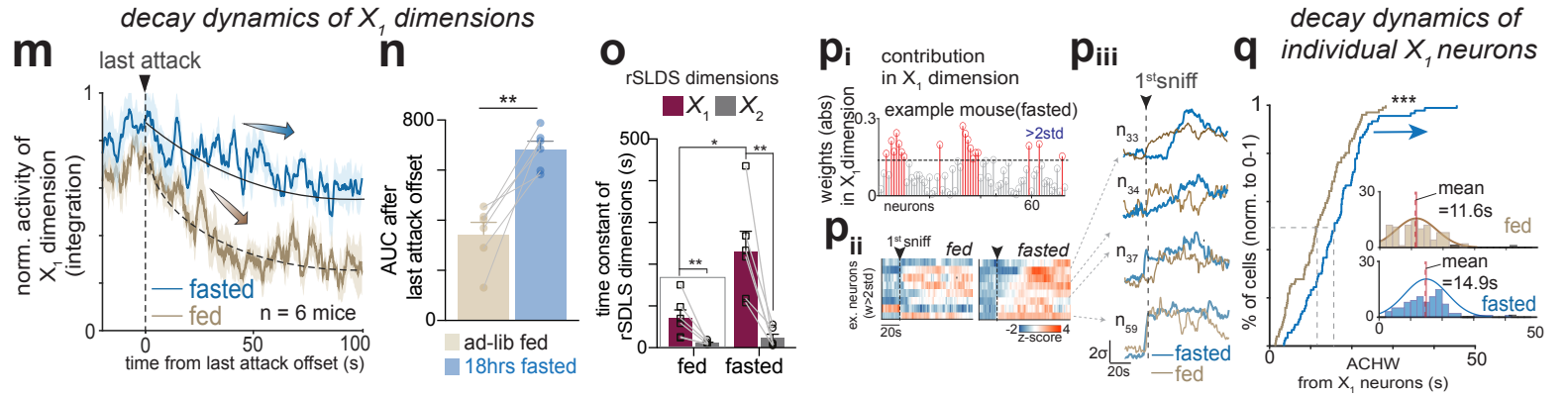

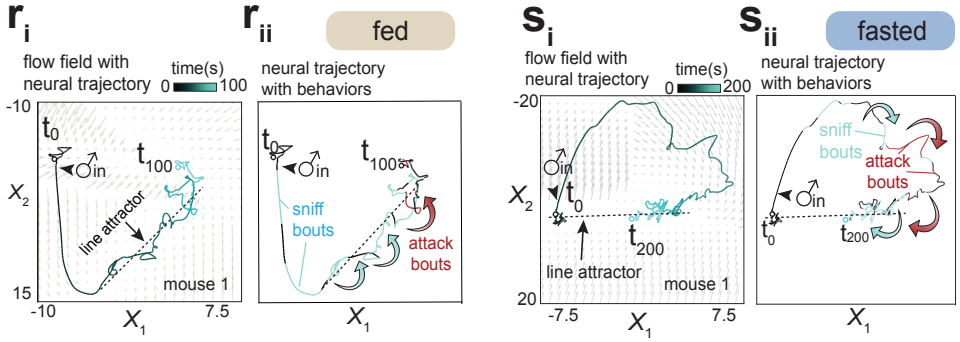

Fig. 2 | Moderate fasting enhances ramping and persistence in a VMHvl^{Esr1} latent slow mode.

(a) (left) Imaging preparation and (right) representative histological section showing GCaMP8m expression (green) and GRIN lens implantation site.

(**b**) Representative imaging planes from longitudinal *in vivo* calcium imaging; color code indicates energy state (above) and mouse number for analysis (below).

(**c-d**) Rasters of VMHvl^{Esr1} neuron activity and resident behavior from a representative fed (**c**) or 18-hr fasted (**d**) mouse, aligned to intruder entry. “fed” and “fasted” above the baseline raster indicate pre-trial treatment.
(**e**) rSLDS model performance as cvR^2 for *ad libitum*-fed and 18-hr fasted conditions.
(**f-g**) Activity of rSLDS latent dimensions aligned with behaviors in a representative *ad libitum*-fed (**f**) and 18-hr fasted (**g**) mouse. Burgundy and gray curves indicate the X_1 and X_2 dimensions, respectively.
(**h-i**) Behavior-triggered average (BTA) of rSLDS dimensions (X_1-burgundy, X_2-gray) aligned to the first sniffing bout in the fed (**h**) or 18-hr fasted (**i**) states across mice (n = 6 mice).
(**j**) BTA of X_1 dimension aligned to first attack in 18-hr fasted vs. fed states (n = 6 mice)**.** Inset: Slope of the ramping segment from (**j_{ii}**) calculated from time of first sniff. See also **Extended Data Fig. 4d**.
(**k**) Correlation between time-to-peak of the X_1 integration dimension and latency from first sniff to the first attack (linear regression, $R^2 = 0.978$, ****$p < 0.0001$). Individual mice are color-coded.
(**l**) Schematic summary of results in (**j-k**) and **Extended Data Fig. 4b-f**.
(**m**) BTA of X_1 dimension aligned to the offset of the final attack bout. Dashed lines: exponential curve-fit of mean activity.
(**n**) Area under the curves (AUC) in (**m**) for 100s after the last attack offset.
(**o**) Time constants of rSLDS dimensions.
(**p**) Dynamics of individual X_1-weighted neurons. (**p_i**) Stem plot of individual cell weights from 18-hr fasted mice**;** red circles, weights >2SD; (**p_{ii}**) Activity of X_1 -weighted neurons in fed (left) vs. 18-hr fasted (right) condition; (**p_{iii}**) Representative traces of neurons from (**p_{ii}**), aligned to the first sniffing bout.
(**q**) ECDF of average autocorrelation half-widths (ACHWs) for X_1-weighted neurons’ activity during male-male interactions (n=6 mice). See also **Extended Data Fig. 3g-j**.
(**r-s**) Representative flow fields of rSLDS models in (**f-g**) with neural trajectories color-coded by time (**r_i, s_i)** or behaviors (**r_{ii}, s_{ii})** in both fed (**r**) and 18-hr fasted (**s**) states.

*$p<0.05$, ***p*<0.01, ***$p<0.001$. For all figure panels, data are mean ± SEM (n=6 mice). See also **Extended Data Fig. 2, 3 and 4**.

Fig. 3 Prolonged fasting duration reveals biphasic effects on aggression and stability of VMHvl^{Esr1} attractor dynamics.

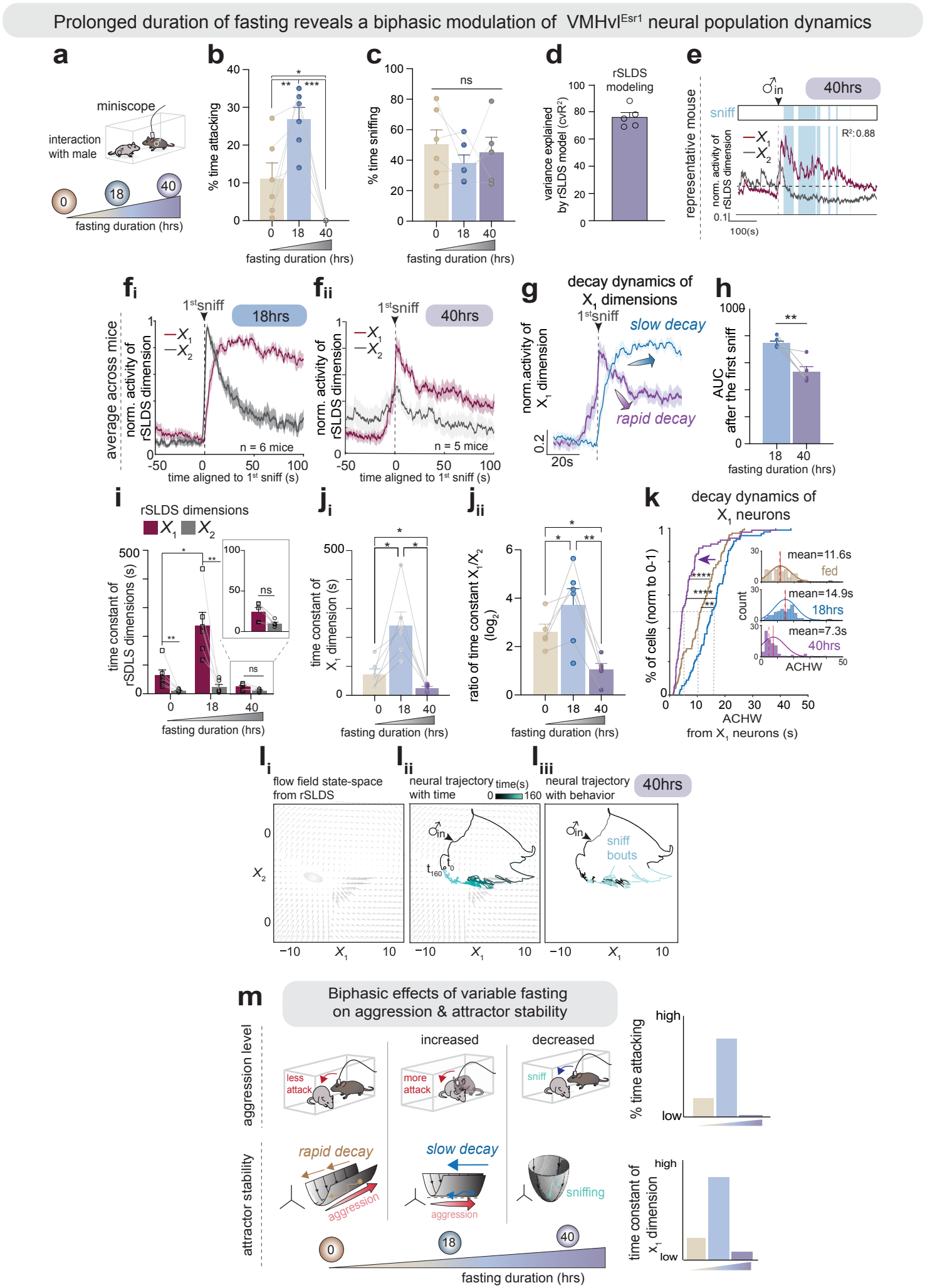

Fig. 3 | Prolonged fasting duration reveals biphasic effects on aggression and stability of VMHvl^{Esr1} attractor dynamics.

(**a**) Schematic of prolonged fasting and its effects on resident-intruder assay.

(**b, c**) Quantification of aggression parameters: (**b**) time spent in attack (%) and (**c**) time spent in sniff (%) across various fasting durations in mice with miniscope. See also **Extended Data Fig. 1d, f and 2a**.

(**d**) rSLDS model performance as cvR^2 for 40-hr fasted conditions.

(**e**) Activity of rSLDS latent dimensions aligned with behaviors in a representative 40-hr fasted mouse. Burgundy and gray curves indicate the X_1 and X_2 dimensions, respectively.

(**f**) BTA of rSLDS dimensions (X_1-burgundy, X_2-gray) aligned to the first sniffing bout in the 18-hr fasted or 40-hr fasted states across mice (n = 6 or 5 mice). **f_i**: Replication of **Fig. 2i** for purposes of comparison.

(**g, h**) X_1 dynamics and activity in 40 hr-fasted mice. (**g**) BTA of X_1 dimension aligned to the first sniffing bout in 18-hr (blue) vs. 40-hr (purple) fasted states; (**h**) AUC in (**g**) for 100s after first sniffing onset.

(**i**) Time constants of rSLDS dimensions across various fasting conditions. i-inset: enlarged time constants in 40-hr fasted condition.

(**j**) Comparison of time constants of X_1 dimension (**j_i**) or ratio of time constants from the X_1 and X_2 dimensions (**j_{ii}**) across fasting conditions.

(**k**) ECDF of ACHWs from X_1-weighted neurons' activity during male-male interactions across fasting conditions.

(l) Representative flow field of rSLDS models (**l_i**) in (**e**) with neural trajectories color-coded by time (**l_{ii}**) or behaviors (l_{iii}) in a 40-hr fasted state.

(**m**) Schematic summary of results in (**b-l**) illustrating the biphasic effect of varying food deprivation levels on the aggressiveness and stability of VMHvl^{Esr1} population dynamics.

*p<0.05, **p<0.01, ***p<0.001, ****p<0.0001; ns, not significant. For all figure panels, data are mean ± SEM (n = 5 or 6 mice).

Fig. 4 Acute, titrated activation of ARC^{AgRP} neurons phenocopies biphasic starvation-induced shifts in aggression-encoding VMH^{Esr1} attractor dynamics

Activation of hunger-encoding ARC^{AgRP} neurons recapitulates the effects of fasting on aggressive behavior

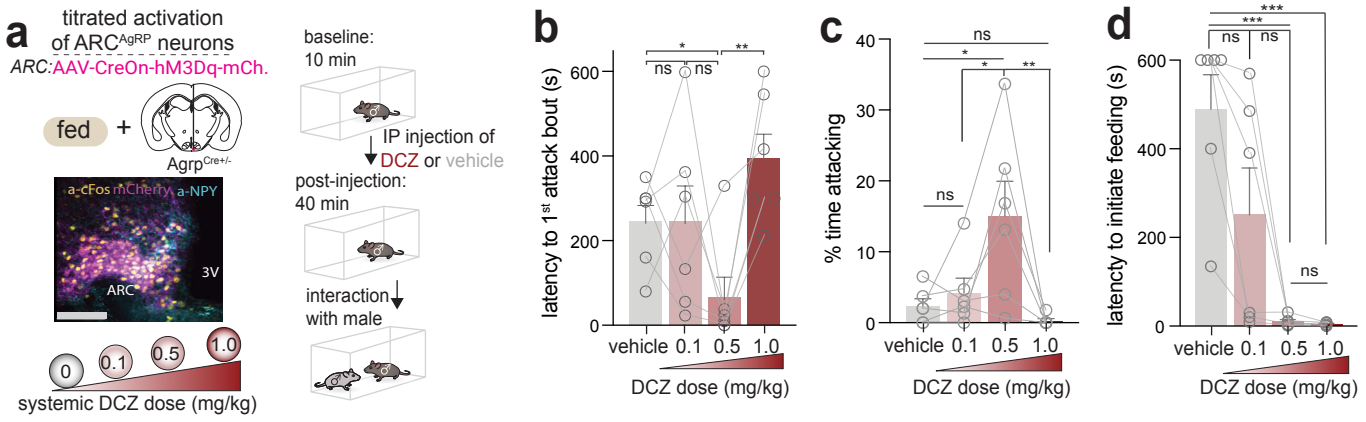

Activation of hunger-encoding ARC^{AgRP} neurons mimics the effects of fasting on attractor dynamics

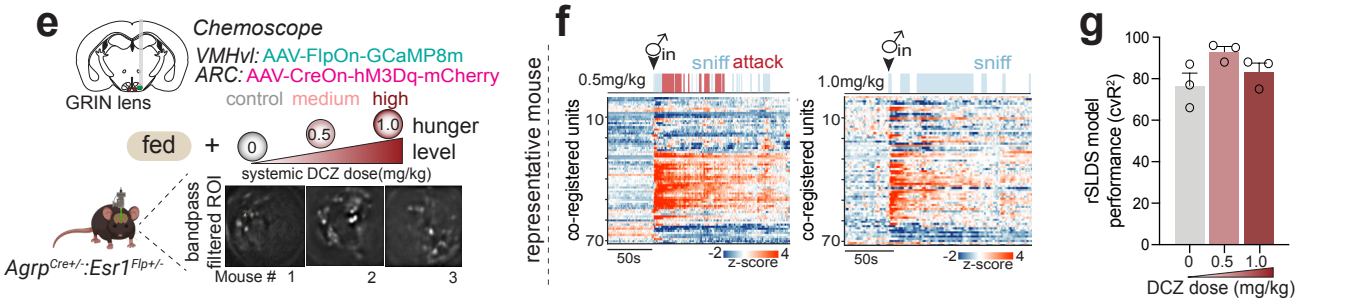

Graded activation of ARC^{AgRP} neurons

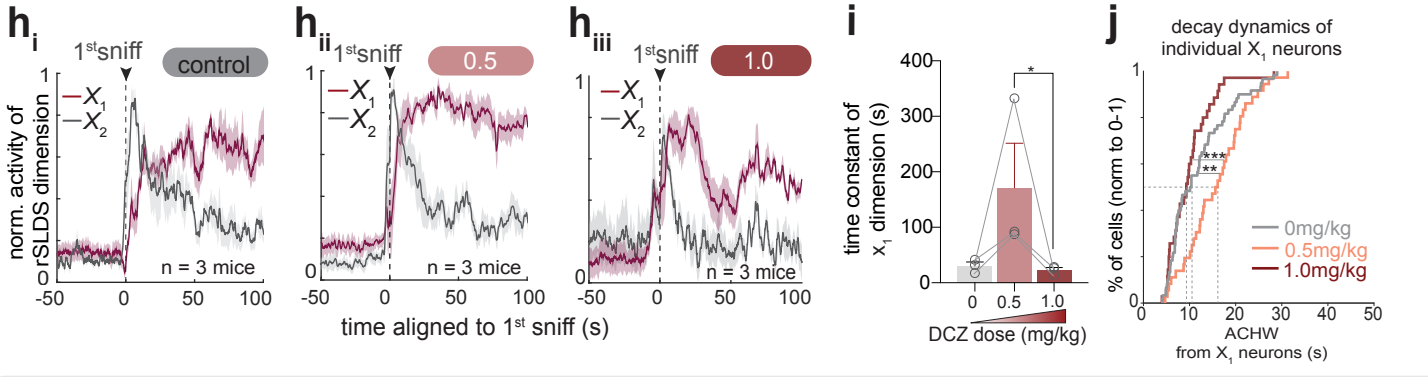

Naturalistic food deprivation

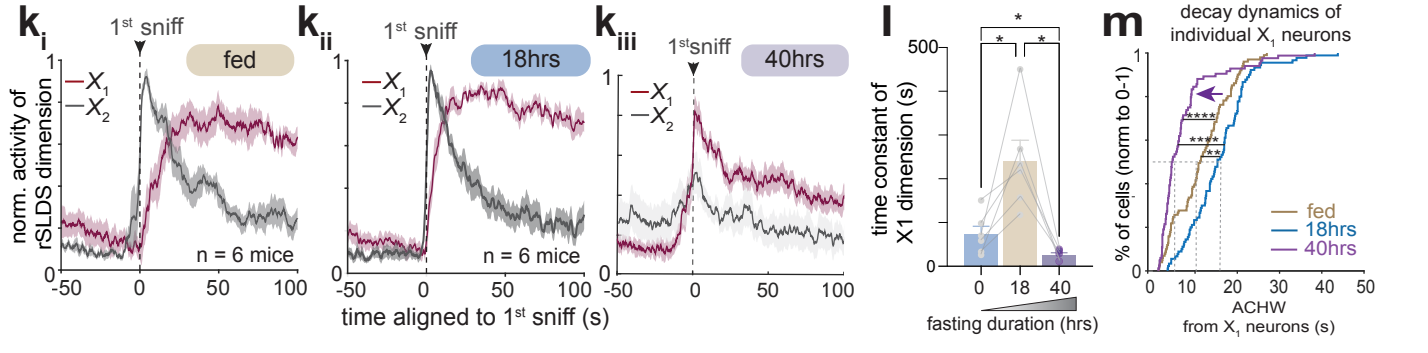

Hunger exerts a flexible, biphasic modulation of aggression levels & attractor stability

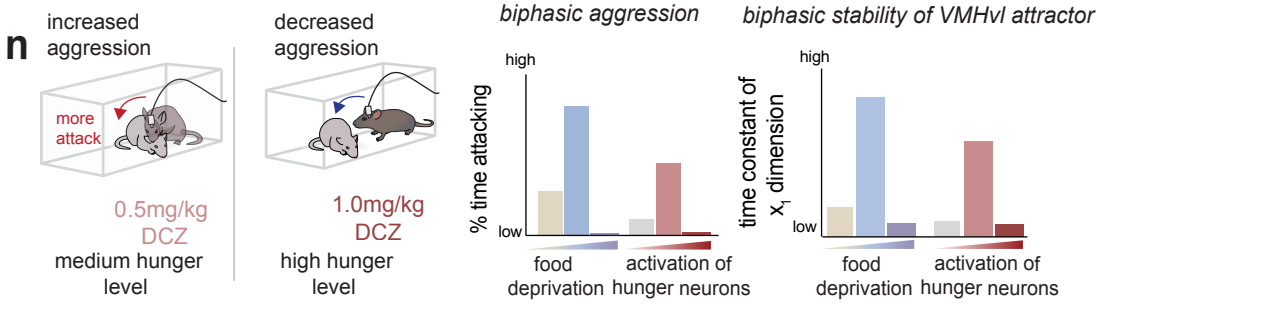

Fig. 4 | Acute, titrated activation of ARC^{AgRP} neurons phenocopies biphasic starvation-induced shifts in aggression-encoding VMH^{Esr1} attractor dynamics.

(**a**) (left) Representative histological section showing hM3Dq-mCherry expression in ARC^{AgRP} neurons and cFos (yellow) induction after 1 mg/kg of DCZ treatment. (right) Schematic of activation of ARC^{AgRP} neurons by systemic DCZ doses, 40-50 min before male-male interaction in *ad libitum*-fed states.

(**b-d**) Quantification of aggression parameters: (**b**) latency to the first attack, (**c**) time spent attacking (%) and (**d**) latency to the first feeding bout during titrated chemogenetic activation of ARC^{AgRP} neurons.

(**e**) Titrated chemogenetic activation of ARC^{AgRP} neurons with miniscope imaging of $VMHvl^{Esr1}$ neuronal activity. FOV from a representative mouse.

(**f**) $VMHvl^{Esr1}$ activity raster (lower, heat map) and resident behavior (upper, raster) from a representative 0.5 mg/kg (left) or 1mg/kg DCZ-treated (right) mouse, aligned to intruder entry. “0.5mg/kg” and “1mg/kg” above the baseline raster indicate pre-trial treatment (see (**a**)).

(**g**) rSLDS model performance as cvR^2 for 0, 0.5, 1.0 mg/kg DCZ conditions (n = 3 mice).

(**h-j**) X_1 dynamics with graded ARC^{AgRP} activation. (**h**) BTA of X_1 and X_2 dimensions, (**i**) Time constants of X_1 dimension, and (**j**) ECDF of ACHWs of X_1-weighted neurons under three different DCZ doses.

(**k-m**) Effects of starvation. (**k**) BTA of X_1 and X_2 dimensions, (**l**) Time constants of X_1 dimensions, and (**m**) EDF of ACHWs of X_1-weighted neurons under naturalistic food deprivation conditions. Data reproduced from **Fig. 2h, i; 3f, j and k** to facilitate comparison with (**h-j**).

(**n**) Schematic illustrating biphasic modulation of aggression and stability of the attractor as a function of levels of food deprivation or artificially induced hunger.

p*<0.05, ***p*<0.01, ****p*<0.001, *****p*<0.0001; ns, not significant. For all figure panels, data are mean ± SEM. See also **Extended Data Figures 5 and 6.

Fig. 5 Persistent aggressiveness during intermittent fighting and feeding in hangry mice

Eating behavior transiently dominates over aggression in the fasted state, when both goal objects are present

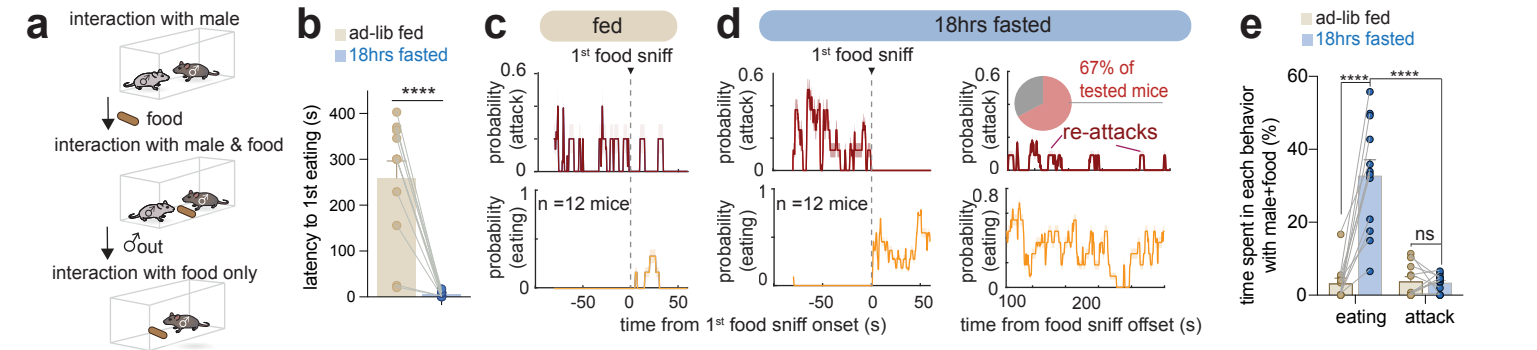

Eating recruits a distinct subpopulation within VMHvl^{Esr1} neurons

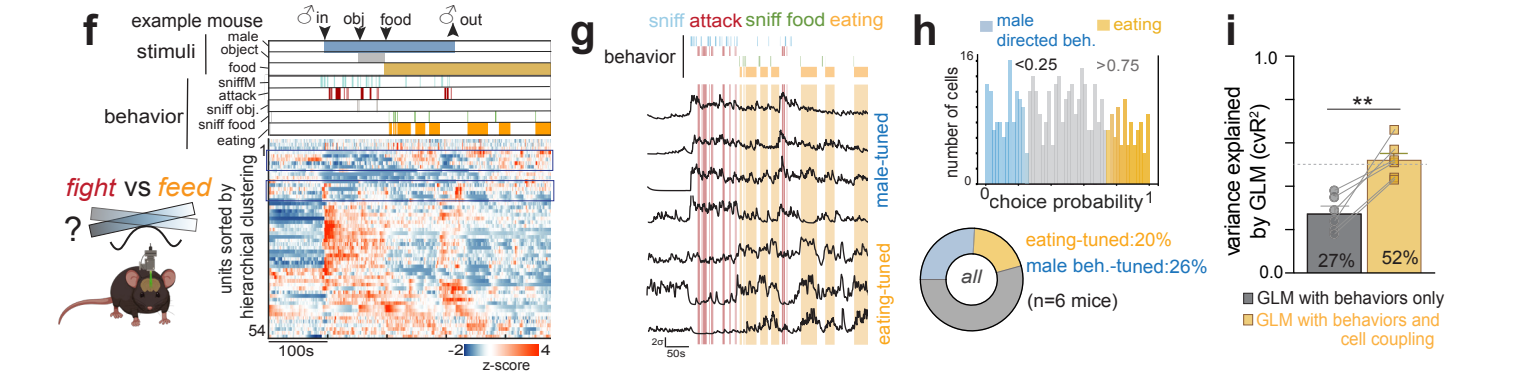

Aggression-encoding attractor dynamics is maintained with orthogonal activations during eating

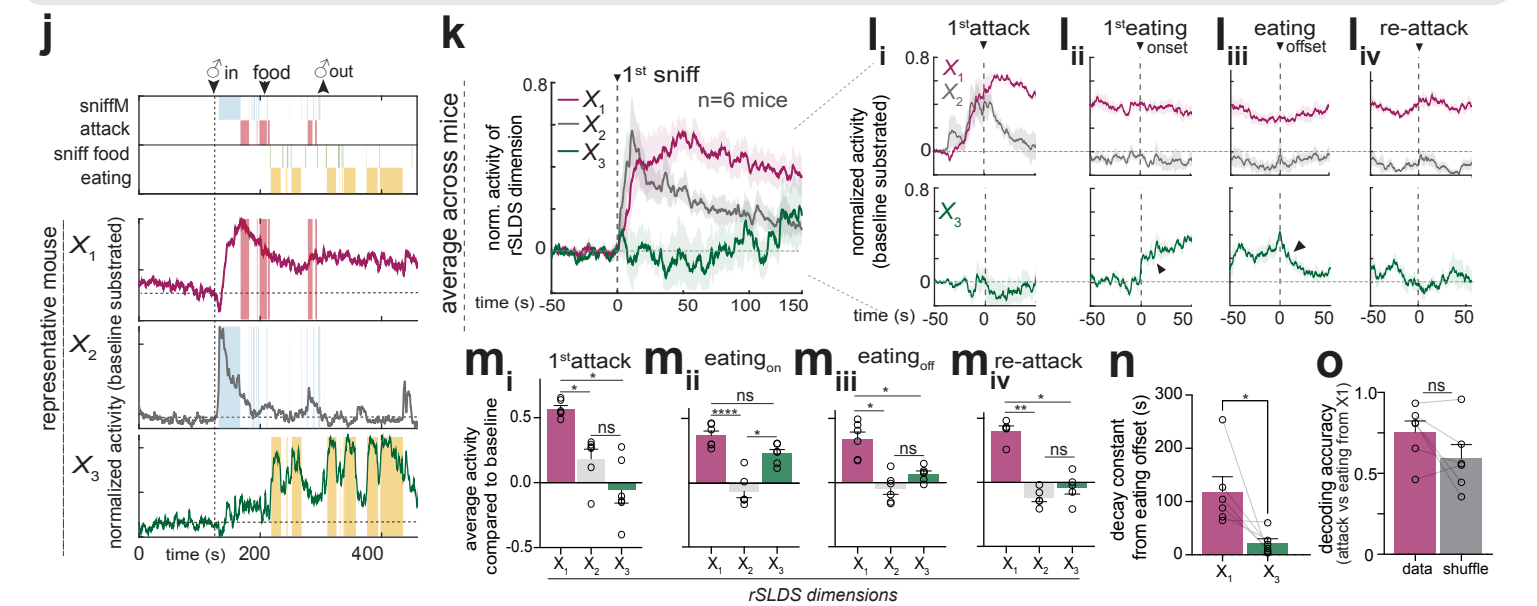

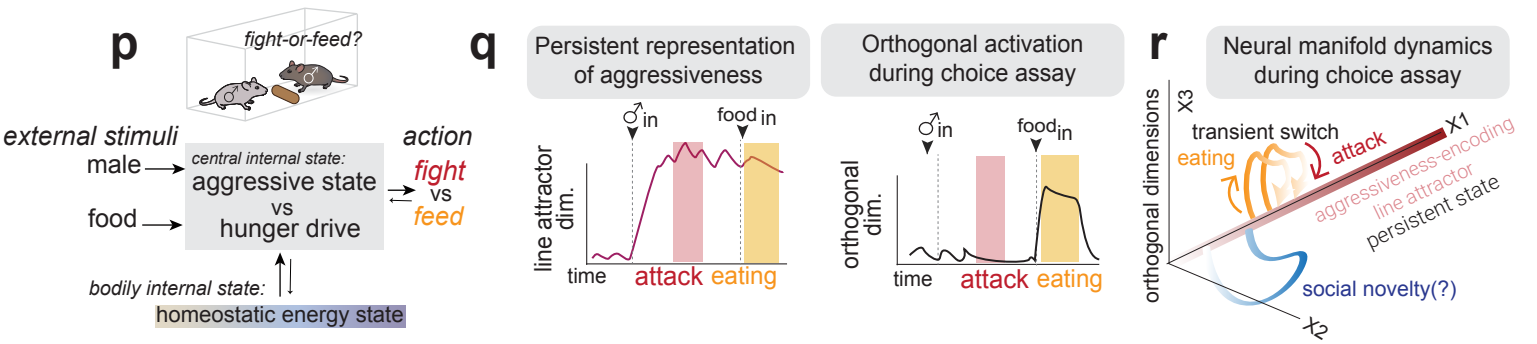

Fig. 5 | Persistent aggressiveness during intermittent fighting and feeding in hangry mice.

(**a**) Schematic illustrating experimental design.
(b) Latency to the first eating bout upon the presentation of a chow pellet in fed vs. 18-hr fasted states.
(**c-d**) Probability of attack (upper) and eating behavior (lower) aligned with first food sniff onset in fed (**c**) and 18-hr fasted states (**d**-left), and aligned with the offset of first food sniff (**d**-right) (n=12 mice).
(**e**) Time spent in eating and attack behaviors during the simultaneous presence of a male and food in fed vs. 18-hr fasted states.
(**f**) Rasters of hierarchically clustered VMHvl^{Esr1} neuron activity (lower, heat map) with a behavior raster (upper) from a representative 8-hr fasted mouse.
(**g**) Representative traces of activity from male-behavior or eating-tuned neurons in (**f**). Colored vertical bars indicate behavior raster.
(**h**) Choice probability for male-directed behavior- vs. eating behavior-tuned cells (upper) and pie chart showing proportion of tuned cells (lower) (n=6 mice).
(**i**) Quantification of cvR^2 for GLM with male or food-related behaviors only vs. behaviors with a cell-coupling term from neural activity (n = 6 mice). See also **Extended Data Fig. 7c**.
(**j**) (lower) First three dimensions of an rSLDS model (X_1-X_3) from a representative mouse, aligned to male entry; (upper) behavior rasters.
(k) BTA of rSLDS dimensions X_1 (burgundy), X_2 (gray), and X_3 (green) dimensions aligned to the first sniff bout (n = 6 mice).
(l) BTAs of baseline-subtracted, normalized activity of X_1 and X_2 (upper row) and X_3 (lower row) aligned to (**l_i**) first attack, (**l_{ii}**) first eating bout, (**l_{iii}**) eating offset, and (**l_{iv}**) re-attack.
(m) Quantification of BTAs in X_1–X_3 dimensions during the four epochs in (**l**). One-way ANOVA with paired post-hoc tests with multiple comparison correction.
(n) Empirically measured decay constants of X_1 vs. X_3 activity following eating offset (**l_{iii}**).
(o) Accuracy of decoding eating vs. attack bouts using X_1 dimension activity (data) is not significantly better than shuffled control, reflecting similar level of X_1 activity during both behaviors (**$l_{i,ii}$**) (n = 6 mice).
(p-r) Schematics summarizing design (**p**) and results (**q, r**) from behavioral choice assay.
(**q**) Summary of activity in X_1 (left) vs. X_3 (right) dimensions during attack vs. eating. (**r**) Neural state-space trajectories of activity in rSLDS latent dimensions during periods of attacking vs. eating.

*p<0.05, **p<0.01, ****p<0.0001; ns, not significant. For all figure panels, data are mean ± SEM. See also **Extended Data Figures 7 and 8**.

Extended Data Fig. 1 | Additional information for Fig. 1

Hunger states modulate innate social behaviors during male-male or male-female interactions

Resident: ad-libitum fed vs 8hr fasted

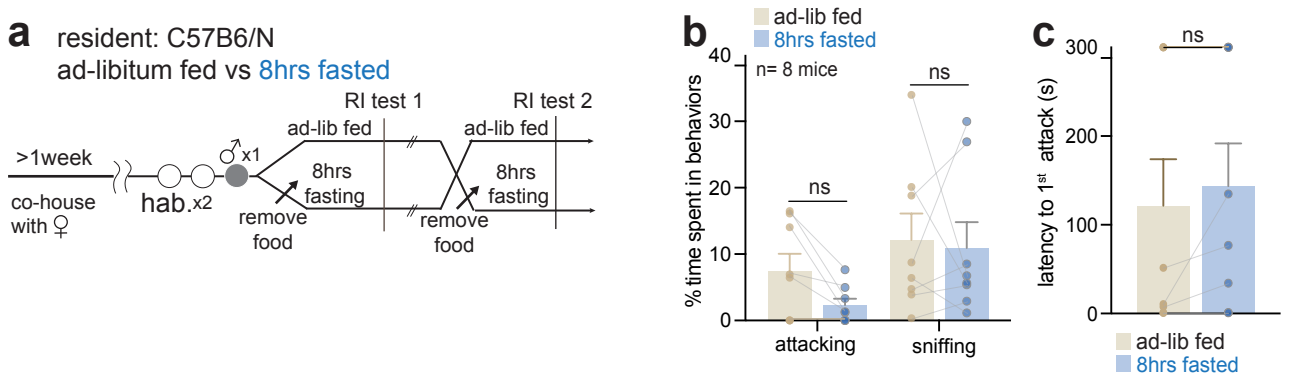

Bi-phasic modulation of aggression by variable fasting duration

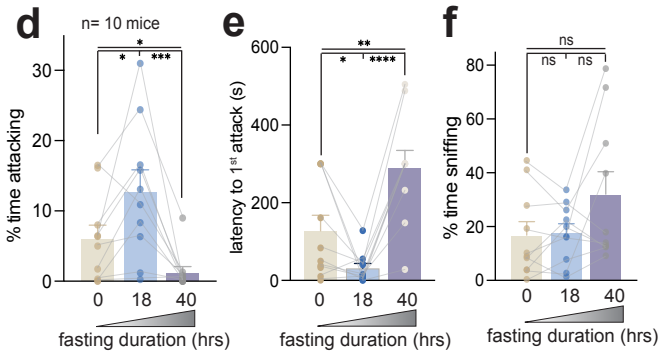

Sexual behaviors during male-female interaction under fed vs. 18 hr fasted states

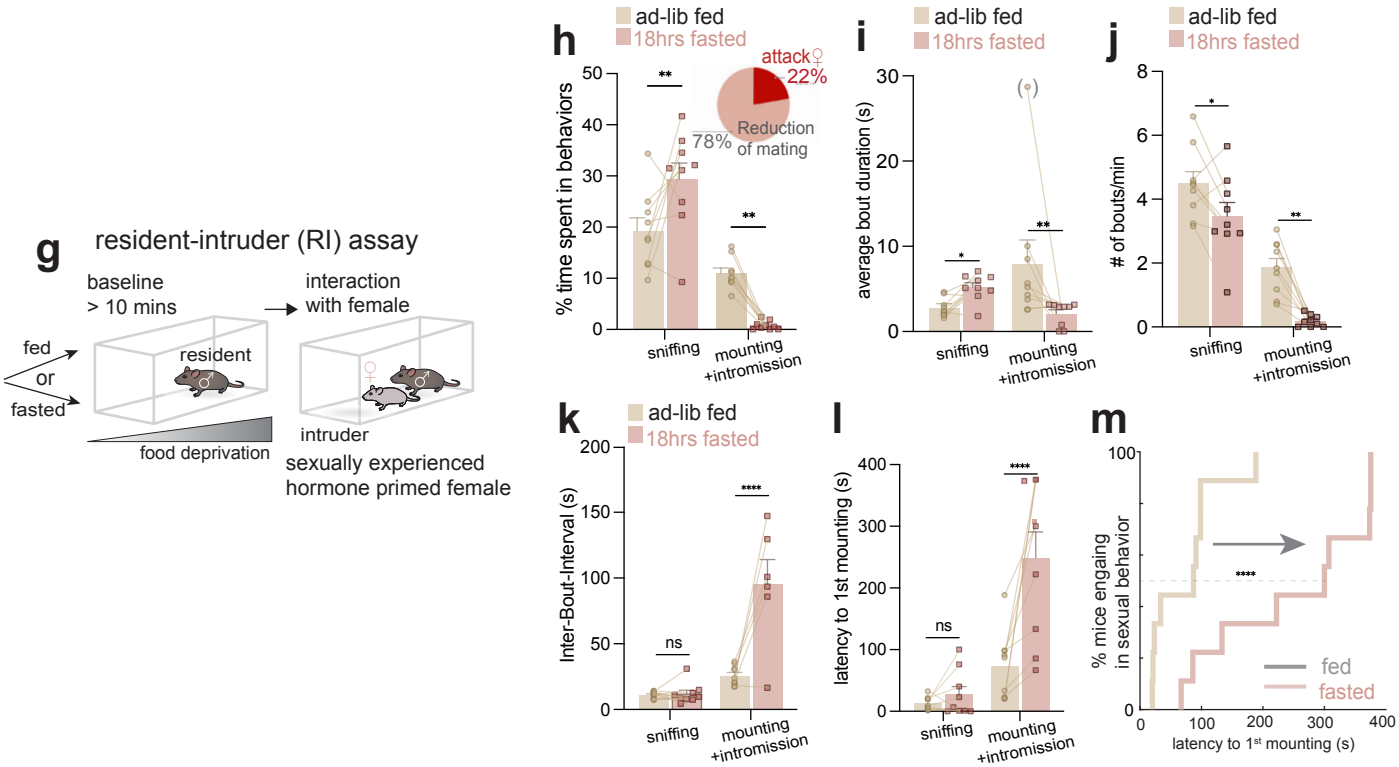

Extended Data Fig. 1 | Hunger states modulate innate social behaviors during male-male or male-female interactions; additional information for Fig. 1.

(a-c) (**a**) Schematic and quantifications of behaviors in fed vs. 8-hour fasted male residents. (**b**) Time spent in attack or sniffing the male intruder (%), and (**c**) latency to the first attack. These males underwent the same conditions as described in Fig. 1, except for 8 hours of food deprivation instead of overnight fasting, with food removal beginning at 9 AM (see Methods for more information, n = 8 mice).

(d-f) Quantification of aggression parameters across *ad libitum*-fed, 18-hr or 40-hr fasted states: (**d**) time spent in attack (%); (**e**) latency to the first attack from the first sniff; (**f**) time spent in sniffing (%). (n = 10 mice).

(g-m) (**g**) Sexual behaviors of resident males during interactions with female intruders in *ad libitum*-fed vs 18-hr fasted states; (**h**) quantifications of time spent sniffing females and female-directed mounting or intromission (%). Inset: 22% of males in the fasted state attacked female intruders; (**i**) average bout duration; (**j**) number of bouts per minute; (**k**) Inter-bout interval; (**l**) latency to the first female-directed mounting, and (**m**) distribution showing the percentage of mice engaging in sexual behaviors for the latency to the first female-directed mounting in fed vs. fasted conditions. For (i), one outlier data point with parentheses, since the difference remained statistically significant even with its exclusion.

*p<0.05, **p<0.01, ***p<0.001, ****p< 0.0001; ns, not significant. For all figure panels, data are mean ± SEM.

Extended Data Fig. 2 | Additional information for Fig. 2.

Aggressive behaviors and tuning properties of VMHvl^{Esr1} neurons across *ad-libitum* fed vs. 18 hr fasted states

Aggressive behaviors in male resident with microendoscope imaging in fed vs. 18hr fasted states (See Fig. 2)

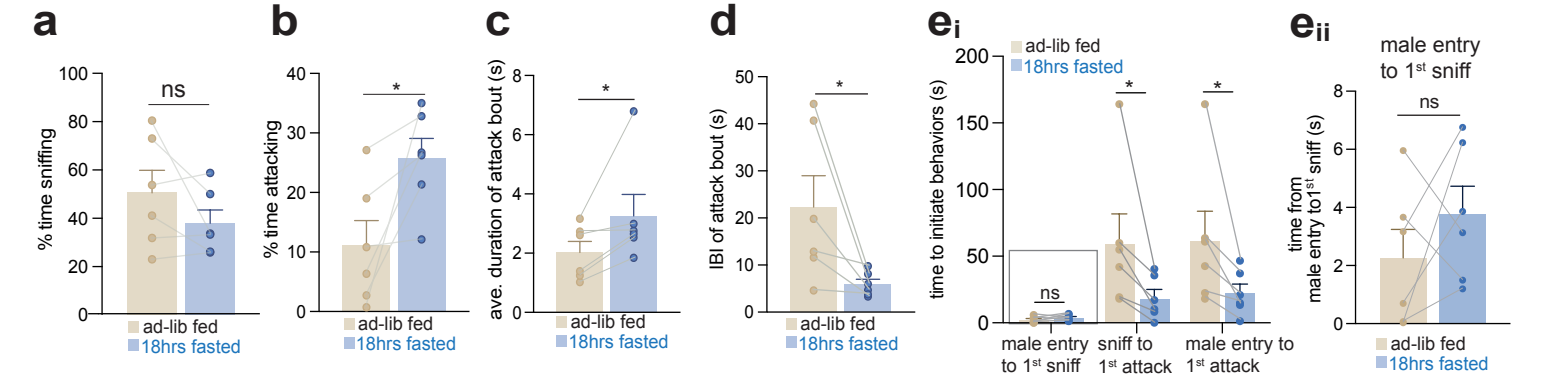

Bulk VMHvl^{Esr1} neural activity levels in fed vs. 18hr fasted states

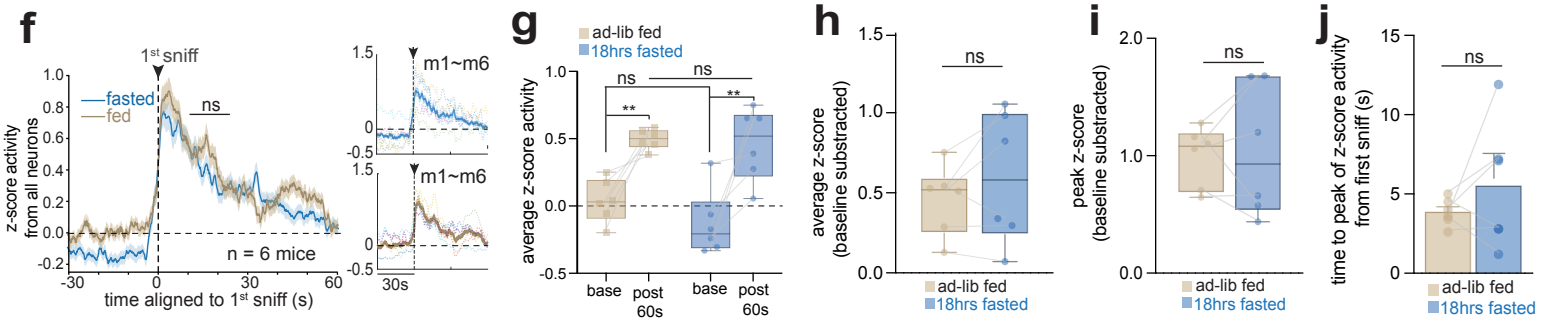

Male-directed behavior tuning properties of VMHvl^{Esr1} neurons in fed vs. 18hr fasted states

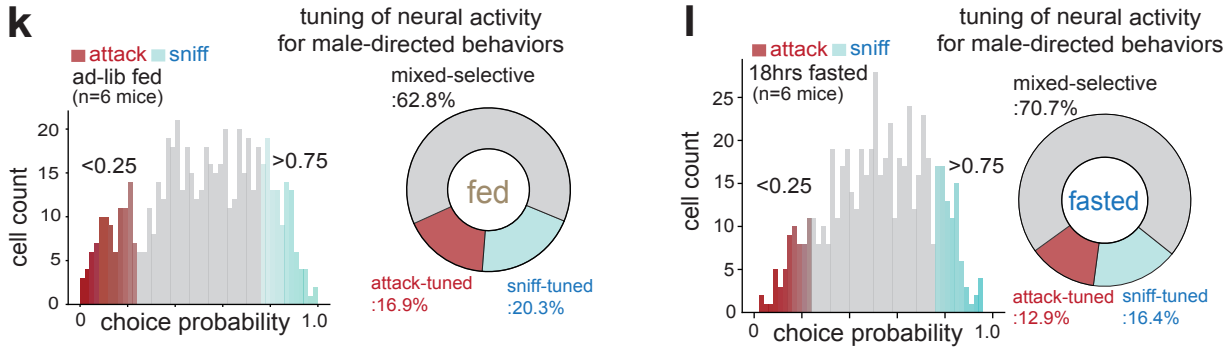

Bulk neural activity levels of *attack-tuned cells* in fed vs. 18hr fasted states

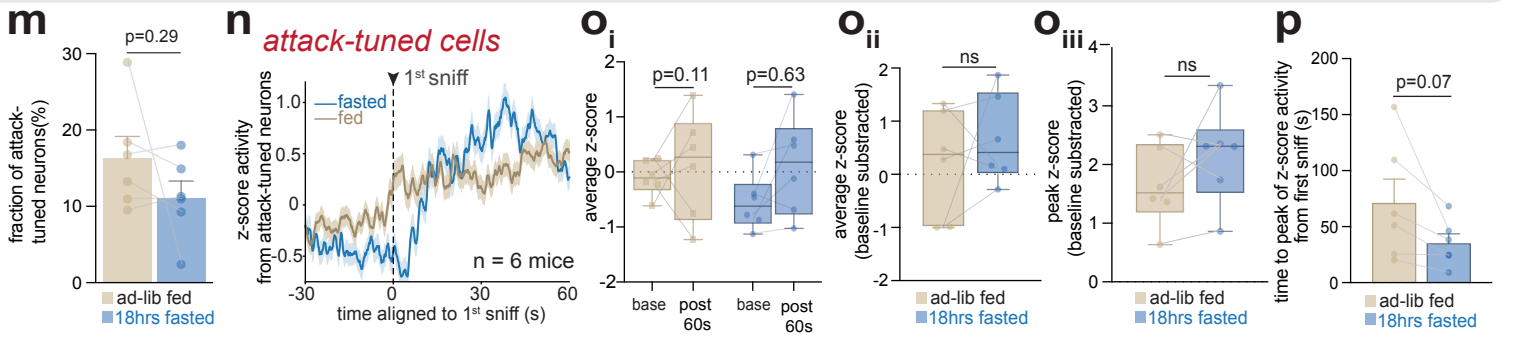

Bulk neural activity levels of *sniffing-tuned cells* in fed vs. 18hr fasted states

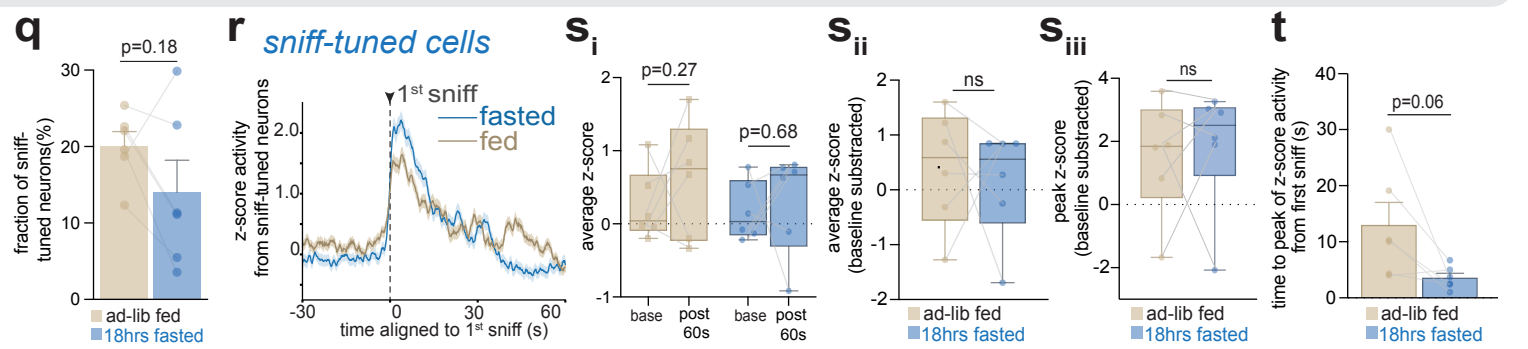

Extended Data Fig. 2 | Aggressive behaviors and tuning properties of VMHvl^{Esr1} neurons in *ad-libitum* fed vs. 18-hr fasted states; additional information for Fig. 2.

(a-e) Quantification of aggression parameters for mice shown in Fig. 2: (**a**) time spent sniffing the male intruder (%); (**b**) time spent in attack (%); (**c**) average attack bout duration; (**d**) Inter-bout interval of attack; (**e**) time from male entry to first sniff and from first sniff to the first attack. $\mathbf{e_{ii}}$: an expanded panel for $\mathbf{e_i}$-box. (n = 6 mice).

(**f**) (left) BTA of bulk VMHvl^{Esr1} activity aligned to the onset of first sniffing showing no significant difference between *ad-libitum* fed and 18-hr fasted states (n = 6 mice). (right) Dashed lines for individual mice.

(**g-h**) (**g**) Average neuronal activity for baseline and 1 min following the first sniff; (**h**) Average baseline subtracted z-score activity between fed vs. 18-hr fasted conditions (ns, $p > 0.05$).

(**i**) Time to peak z-score following first sniffing (ns, $p > 0.05$, paired t-test).

(**j**) BTA of bulk VMHvl^{Esr1} activity aligned to the onset of the first attack for between fed vs. fasted states (ns, $p > 0.05$).

(**k-l**) Choice probability for male-directed sniffing vs. attack behavior and percentage of cells with tuning preference in (**k**) fed and (**l**) fasted states.

(**m, q**) Fraction of neurons for attack-tuned (left) and sniff-tuned (right) across fed (**m**) and fasted (**q**) states.

(**n, r**) BTA of VMHvl^{Esr1} neuronal population tuned to attack vs. sniffing from the choice probability analysis, aligned to the onset of first sniffing between *ad-libitum* fed and 18-hr fasted states (n = 6 mice).

*$p<0.05$; ns, not significant. For all figure panels, data are mean ± SEM.

Extended Data Fig. 3 | Additional information for Fig. 2

Improved GLM fits with cell coupling and enhanced persistence of VMHvl^{Esr1}neurons in fasted mice

Gerneralized Linear encoding Model with behavior or behavior+cell coupling regressor

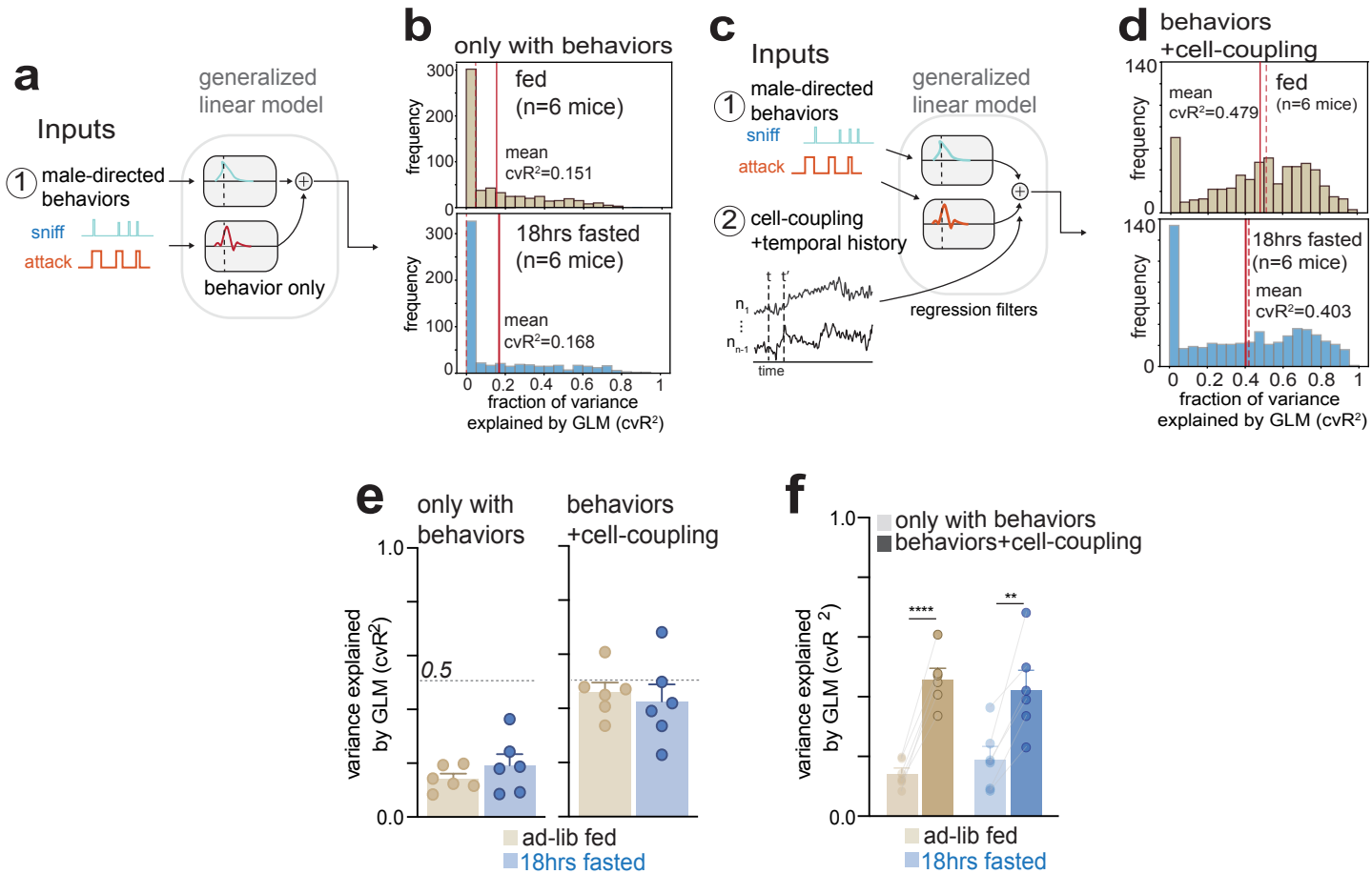

Persistence of VMHvl^{Esr1} neural activity with GCaMP8m

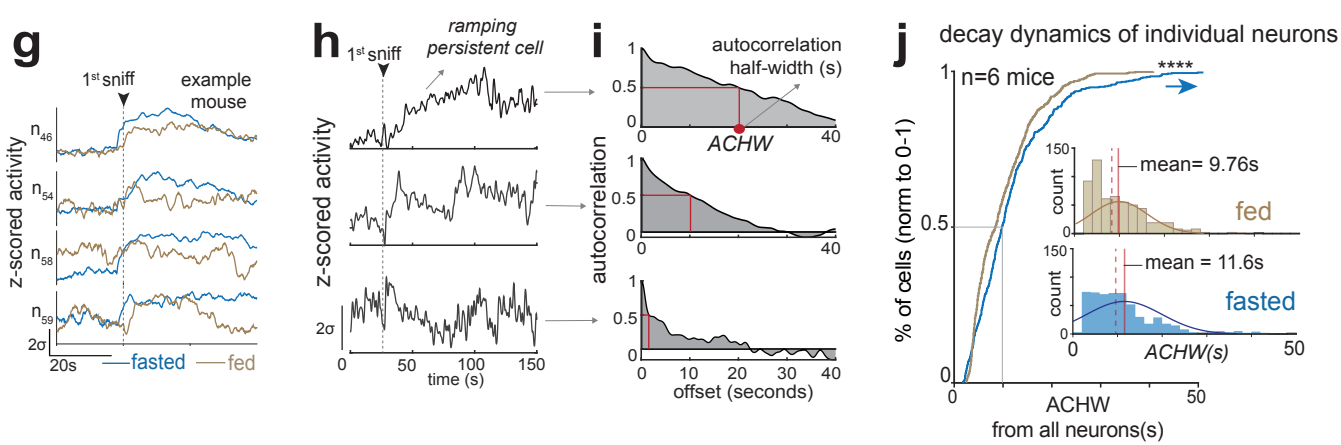

Extended Data Fig. 3 | Improved GLM fits with cell coupling and enhanced persistence of VMHvl^{Esr1} neurons; additional information for Fig. 2.

(**a**) Schematics of a GLM to predict individual cell activity from a behavior regressor.

(**b**) Histogram with variance explained (cvR^2) across all neurons, n=6 mice from behavior-only GLM in the fed (above) and fasted (below) states. Solid line: mean; dashed line: median value.

(**c**) Schematics of GLM to predict individual cell activity from behavior and cell-cell coupling.

(**d**) Histogram with cvR^2 across all neurons, n=6 mice from behavior + cell-coupling GLM in fed (above) and fasted (below) states. Solid line: mean; dashed line: median value.
(**e-f**) Quantification of cvR^2 in GLM with behavior + cell-coupling compared to the behavior-only regressor.

(**g**) Individual neural traces between *ad-libitum* fed vs. fasted states, showing persistence during male-male interaction with the GCaMP8m indicator, blue: fasted, brown: fed state.

(**h-i**) Individual example neural traces with the most extended (upper, 20s), medium (middle, 10s), and shorter (lower, 5s) ACHW.

(**j**) Distribution of cells for ACHW in fed vs. 18-hr fasted state for 6 mice. Histogram of ACHW (inset). Paired or unpaired t-test,

$^{**}p<0.01$, $^{***}p<0.001$, $^{****}p<0.0001$; ns, not significant. For all figure panels, data are mean ± SEM.

Extended Data Fig. 4 | Additional information for Fig. 2

Enhanced ramping and stability of aggression-encoding VMHvl^{Esr1} attractor dynamics in 18 hr fasted state

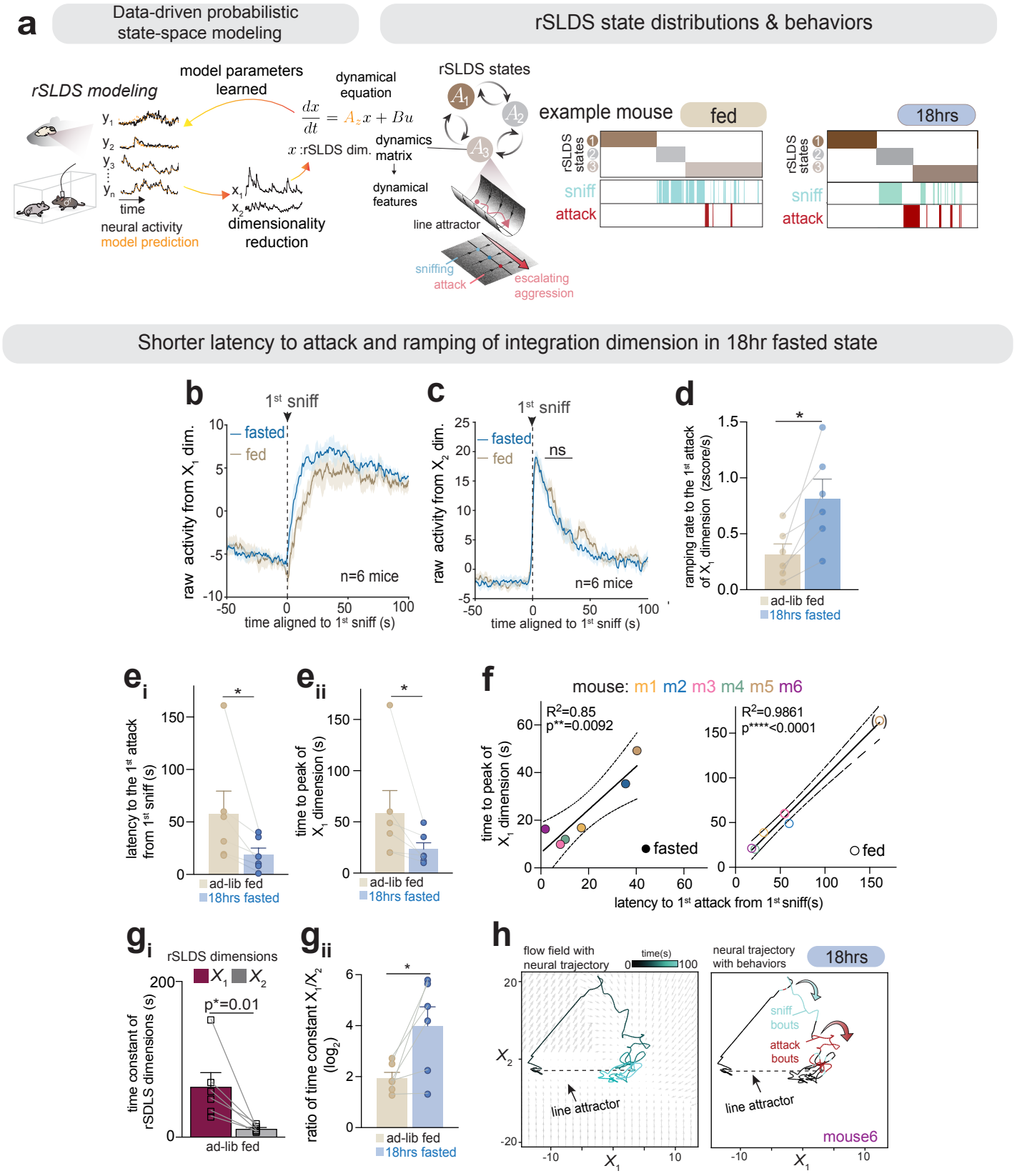

Extended Data Fig. 4 | Enhanced ramping and stability of aggression-encoding VMHvl^{Esr1} attractor dynamics in 18-hr fasted state; additional information for Fig. 2.

(**a**) (left) Schematics of rSLDS modeling. (right) Discrete states of rSLDS model and behavior raster in **Fig. 2f, g** from fed and fasted states.

(**b-c**) BTA of non-normalized activity in the X_1 dimension (**b**) or X_2 dimension (**c**), aligned to the first attack in the fasted and fed conditions (n = 6 mice). Compare with **Fig. 2h, i**.

(**d**) Ramping rate of the X_1 dimension in **Fig. 2j$_{ii}$**.

(**e**) Quantifications of (**e$_i$**) latency to the first attack and (**e$_{ii}$**) time to peak activity in the integration dimension from the first sniff in fed vs. fasted states.

(**f**) Correlation between the time to peak integration dimension and the latency to the first attack in the fasted state (left, closed circles) and the fed state (right, closed circles). Individual mice are color-coded. $R^2 = 0.85$, $^{**}p = 0.0092$ (left); $R^2 = 0.98$, $^{****}p < 0.0001$ (right). One data point with () in the right panel, as the statistical significance did not change even with its exclusion.

(**g**) Quantifications of the ratio between time constants from X_1 and X_2 dimensions between fed vs. 18-hr fasted.

(**h**) Another example of flow field of rSLDS model with neural trajectory in the fasted state.

$^{*}p<0.05$, $^{**}p<0.01$, $^{***}p<0.001$; ns, not significant. For all figure panels, data are mean ± SEM.

Extended Data Fig. 5 | Additional information for Fig. 4

Acute, titrated activation of ARC^{AgRP} neurons shifts aggression-encoding VMH^{Esr1} attractor dynamics

Activation of hunger-encoding ARC^{AgRP} neurons mimics the effects of fasting on attractor dynamics

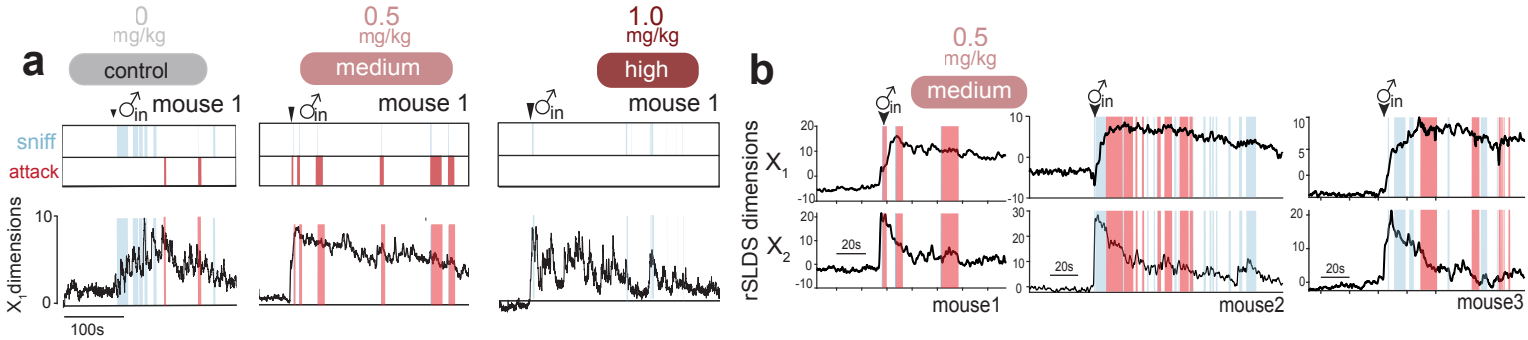

Ramping dynamics of VMHvl^{Esr1} neural population dynamics under control vs medium-dose activation

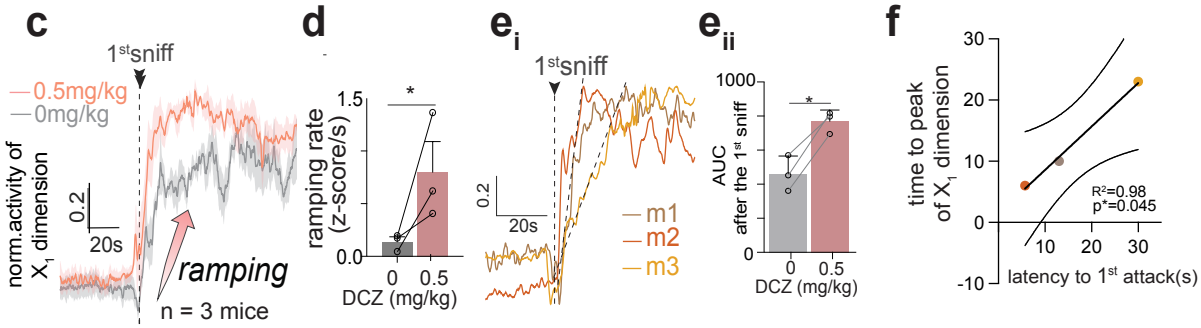

Stability of VMHvl^{Esr1} neural population dynamics

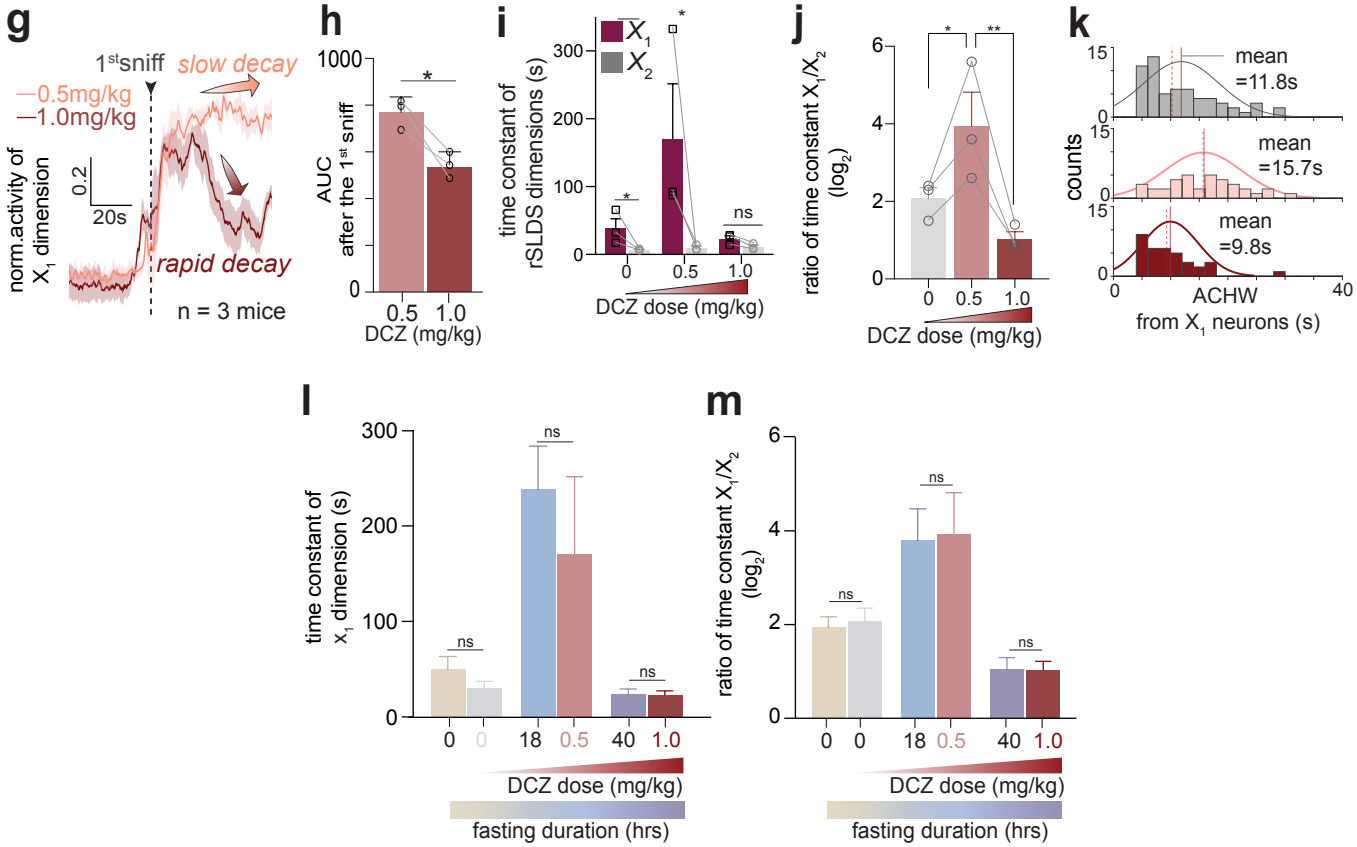

Extended Data Fig. 5 | Acute, titrated activation of ARC^{AgRP} neurons shifts aggression-encoding VMH^{Esr1} attractor dynamics; additional information for Fig. 4.

(**a**) Representative traces of X_1 dimension at each dose for ARC^{AgRP} neuronal activation from a representative mouse with male-directed behavior raster.

(**b**) Representative traces of X_1 and X_2 dimensions in medium-dose conditions showing rapid ramping and persistent activity in the X_1 dimension with a color-coded raster of sniffing (blue) or attack (red) behaviors across mice.

(**c**) BTA of X_1 dimensions comparing saline (gray) vs medium-dose (pink) conditions, highlighting the accelerated ramping in the medium dose.

(**d**) Quantification of the ramping rate from (**c**).

(**e**) Individual traces of X_1 dimension at the medium level of activation with rapid ramping (**e**$_i$) and AUC calculated for 100s after the first sniff (**e**$_{ii}$).

(**f**) Correlation between the time to the peak of the X_1 dimension and the latency to the first attack from the first sniff bout.

(**g-h**) BTA of X_1 dimensions comparing medium vs. high-dose condition: (**g**) difference in persistence of the first dimension of rSLDS; (**h**) quantifications of AUC after the first sniff.

(**i**) Time constant from X_1 and X_2 dimensions across three different conditions of chemogenetic activation of ARC^{AgRP} neurons.

(**j**) Quantification of the ratio between the time constants of X_1 and X_2 dimensions.

(**k**) Histogram of ACHWs across control, medium, and high-dose conditions in **Fig. 4j**.

(**l-m**) Quantification of (**l**) time constant for the X_1 dimension or (**m**) ratio between time constants for X_1 and X_2 dimensions across naturalistic food deprivation or activation of ARC^{AgRP} neuronal activity to induce hunger drive.

*p<0.05, **p<0.01; ns, not significant. For all figure panels, data are mean ± SEM.

Extended Data Fig. 6 | Additional information for Fig. 4

Acute, titrated activation of ARC^{AgRP} neurons phenocopies biphasic starvation-induced shifts in aggression-encoding VMH^{Esr1} attractor dynamics

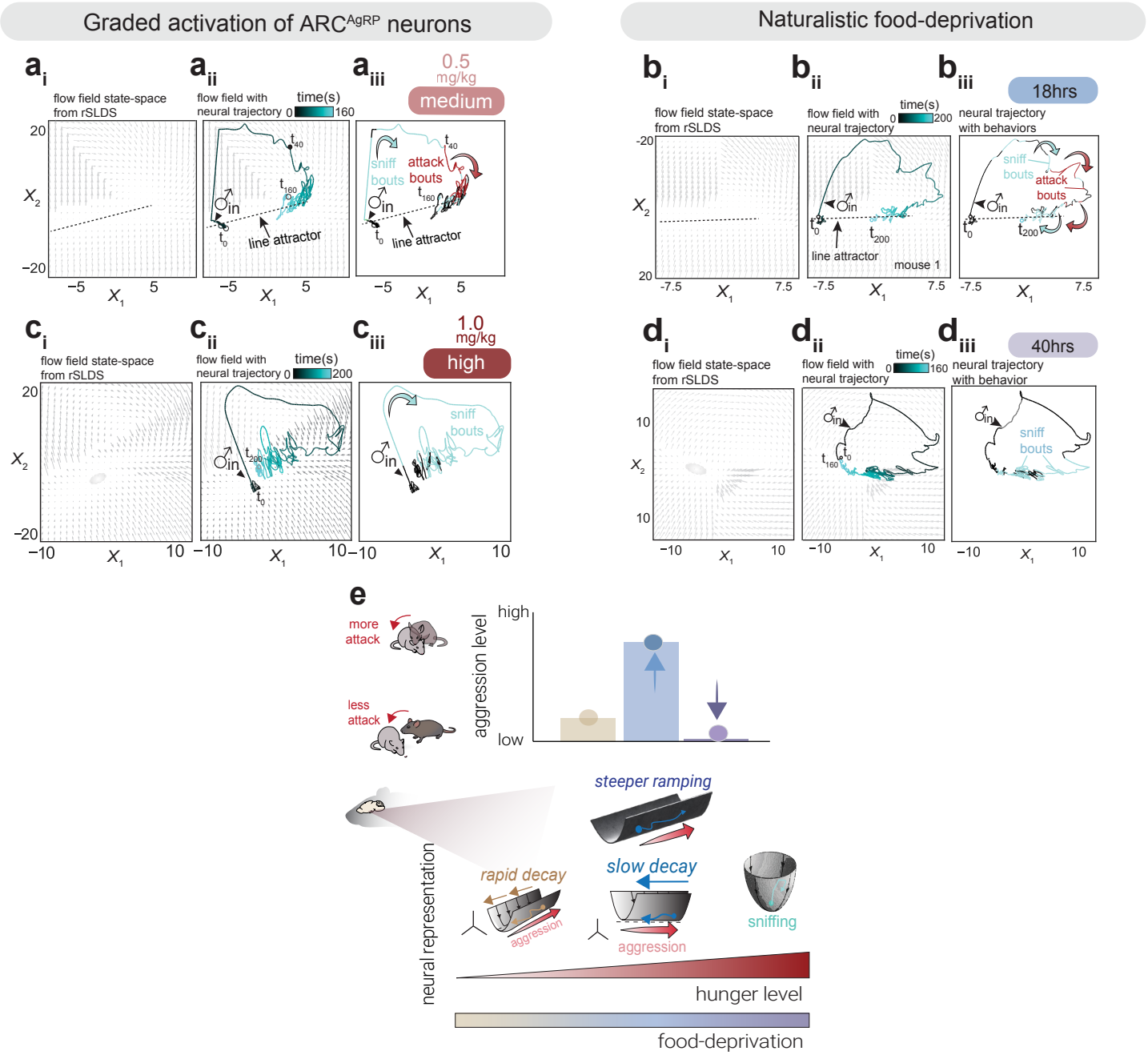

Extended Data Fig. 6 | Acute, titrated activation of ARC^{AgRP} neurons phenocopies biphasic starvation-induced shifts in aggression-encoding VMH^{Esr1} attractor dynamics; additional information for Fig. 4.

(**a-d**) Representative flow fields with trajectory colored by time (middle) or behaviors (right) from rSLDS-modeled attractor dynamics under naturalistic food deprivation conditions for 18-hr (**a**) or 40-hr (**c**) and chemogenetic activation of ARC^{AgRP} neuronal activity at medium (**b**) or high-dose conditions (**d**).

(**e**) Schematic summarizing the effects of various hunger levels on aggression and aggressiveness-encoding VMHvl^{Esr1} neural population dynamics.

Extended Data Fig. 7 | Additional information for Fig. 5

A competing action for food elicits orthogonal perturbations in the VMHvl^{Esr1} attractor dynamics, with distinct tuning properties

Distribution of behaviors under competing states with food

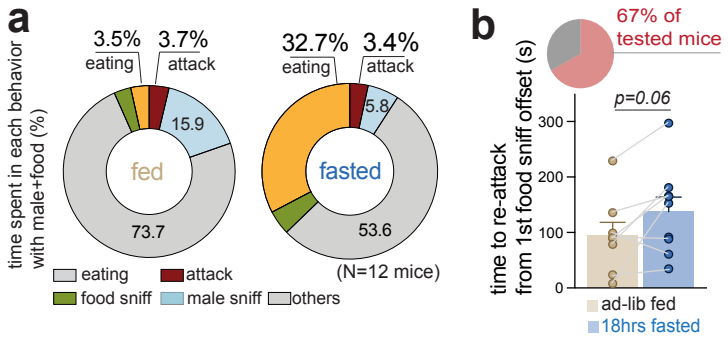

Male or food-directed behavior tuning properties of VMHvl neurons

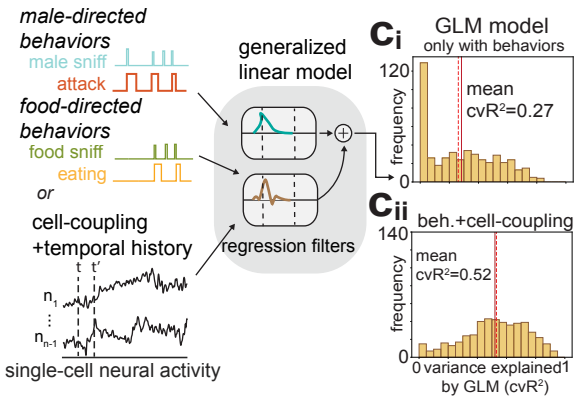

rSLDS modeling under competiting aggressive and hunger states with presence of male and food

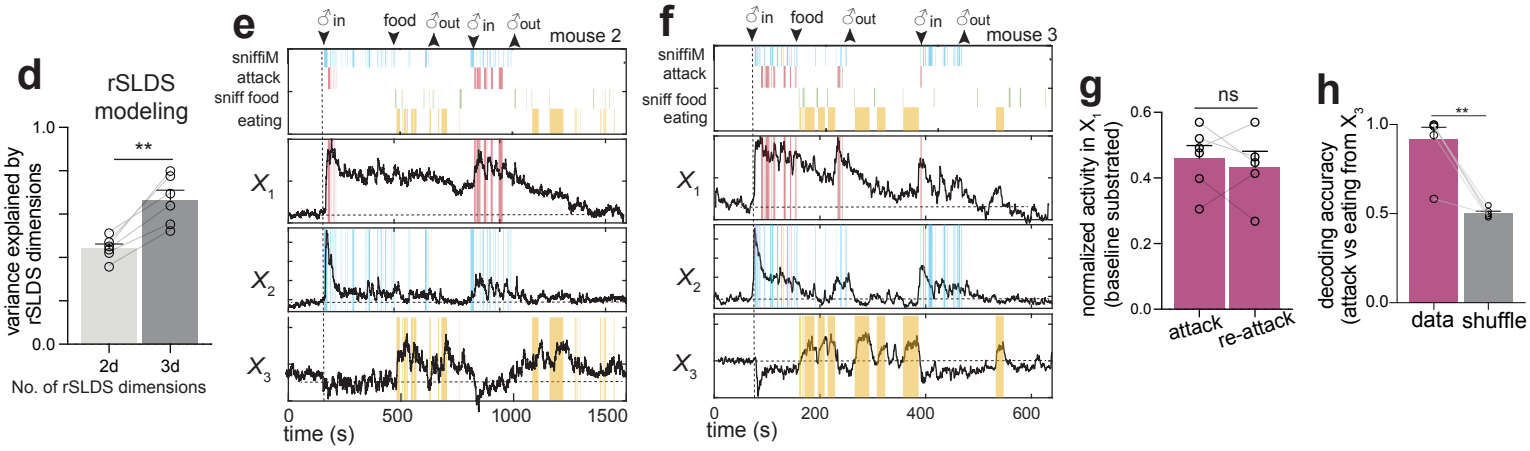

Single cell analysis of rSLDS dimensions

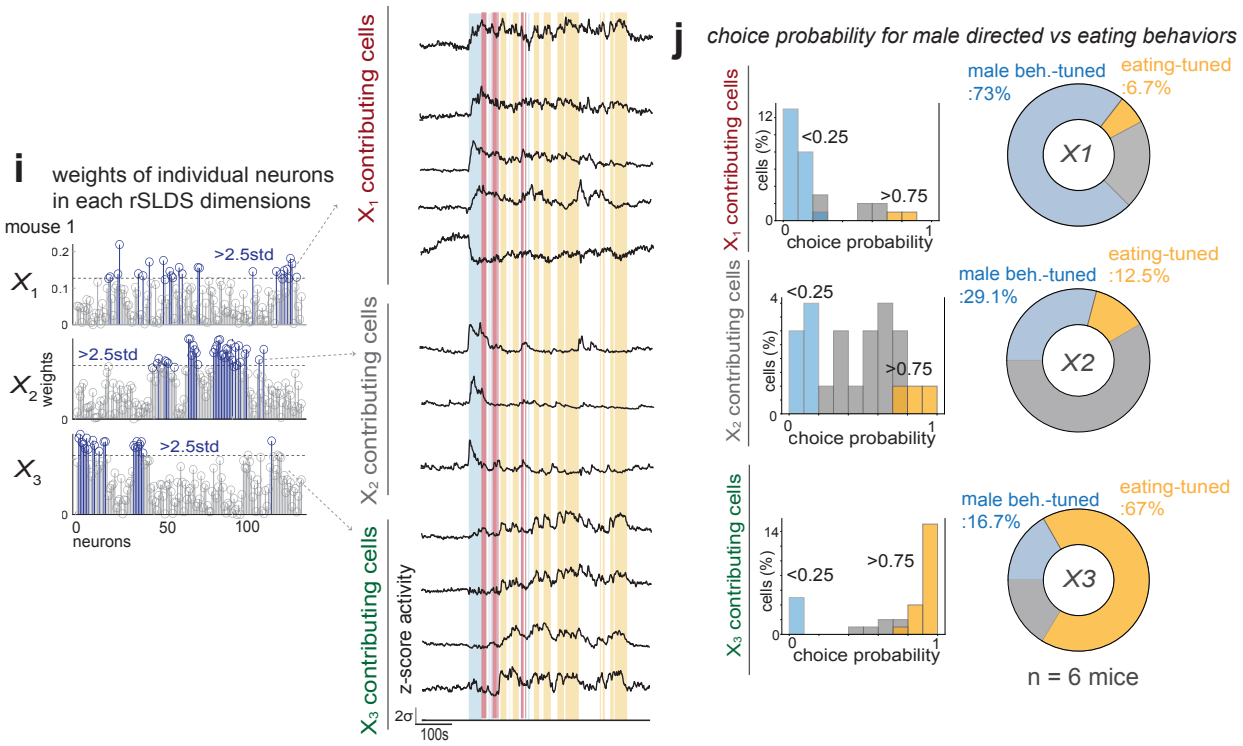

Extended Data Fig. 7 | A competing action for food elicits orthogonal perturbations in the VMHvl^{Esr1} attractor dynamics, with distinct tuning properties; additional information for Fig. 5.

(**a**) Pie charts of distribution of behaviors when males and food are present together in the fed state (left) and fasted state (right).

(**b**) Quantification of time to re-attack from the first food sniff offset in the fasted state. 67% of tested mice exhibited re-attack after transitioning to eating behavior (right).

(**c**) Histogram of GLMs with male or food-related behaviors only (**c$_i$**) and behaviors with cell-to-cell coupling from the neural activity (**c$_{ii}$**) of the fasting condition. Solid lines: mean values; dashed lines: median values.

(**d**) Quantification of rSLDS model performance using two vs. three dimensions.

(**e-f**) Representative traces of rSLDS dimensions (upper, X_1; middle, X_2; below, X_3) for (**e**) another mouse and (**f**) the mouse shown in **Fig. 5 f, g**.

(**g**) (left) X1-X3 weights for each individual cell in the example mouse used in **Fig. 5j**. (right) Representative traces of single-cell activity from X_1, X_2, and X_3-weighted neurons.

(h) Choice-probability of male-directed behaviors (attack + sniff) vs. feeding (eating) in the fasted state in X_1, X_2, X_3-weighted neurons (n = 6 mice).

(**i**) Quantification of X_1 activity after attack or re-attack, reused from **Fig. 5m$_i$ and 5m$_{iv}$**.

(**j**) Decoding accuracy distinguishing eating vs. attack bouts in real vs. shuffled data from the X_3 dimension (n = 6 mice). $^{**}p<0.01$; ns, not significant. For all figure panels, data are mean ± SEM.

Extended Data Fig. 8 | Additional information for Fig. 5

Trajectories in rSLDS state space reveal distinct manifolds, with a persistent and attractive aggressive state under drive for feeding in the VMHvl^{Esr1} neural population

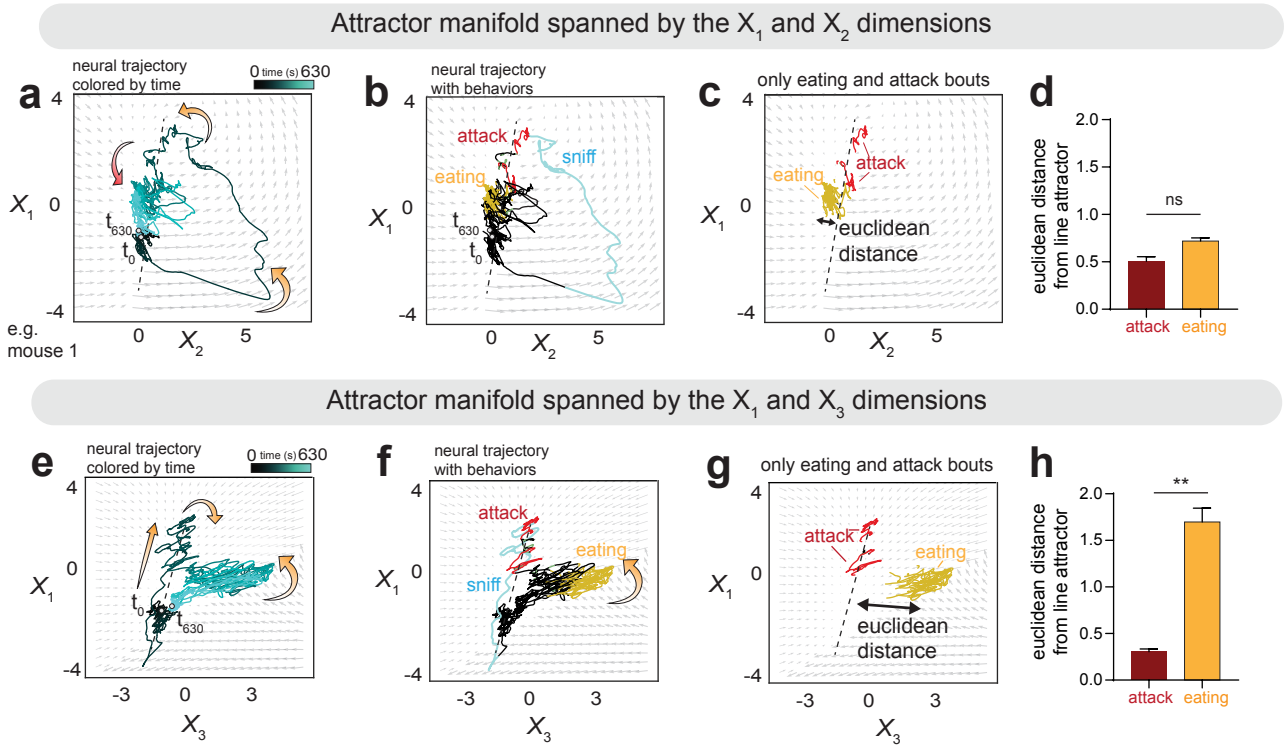

Extended Data Fig. 8 | Trajectories in rSLDS state space reveal distinct manifolds, with a persistent and attractive aggressive state under drive for feeding in the VMHvl^{Esr1} neural population; additional information for Fig. 5.

(**a-c**) rSLDS modeling based on the state space of the X_1-X_2 dimensions with trajectories (**a**) colored by time, (**b**) by behavior, and (**c**) trajectories during attack and eating behavior bouts.

(**d**) Quantification of Euclidean distance in **Fig. 8c** from the line attractor for attack and eating behavior bouts.

(**e-g**) Neural state space of the X_1-X_3 dimensions with trajectories: (**e**) colored by time, (**f**) colored by behavior; (**g**) only trajectories during attack and eating.

(**h**) Quantification of Euclidean distance in **Fig. 8g** from the line attractor during attack and eating behavior bouts. $^{**}p<0.01$; ns, not significant.

For all figure panels, data are mean ± SEM.